Effects of Adsorbate Diffusion and Edges in a Transition from Particle to Dendritic Morphology during Silver Electrodeposition

Sohère Dokhan, Dung Di Caprio, Abdelhafed Taleb, Fábio Reis

Effects of Adsorbate Diffusion and Edges in a Transition from Particle to Dendritic Morphology During Silver Electrodeposition

Sohère Dokhan,[*,†,¶] Dung di Caprio,[*,†] Abdelhafed Taleb,[*,†,§] and Fábio D. A. Aarão Reis[*,‡]

†*PSL Research University, Chimie ParisTech - CNRS, Institut de Recherche de Chimie Paris, 75005, Paris, France*

‡*Instituto de Física, Universidade Federal Fluminense, Avenida Litorânea s/n, 24210-340 Niterói, RJ, Brazil*

¶*Unité de Recherche Matériaux, Procédés et Environnement URMPE, Université M'hamed Bougara de Boumerdés, Faculté des Sciences, Boumerdés, Algérie*

§*Sorbonne Universités, 75231, Paris, France*

E-mail: dokhane.sohere@hotmail.com; dung.di-caprio@chimieparistech.psl.fr; abdelhafed.taleb@upmc.fr; fdaar@protonmail.com

Abstract

During silver electrodeposition on Au nanoparticle (NP) covered highly oriented pyrolitic graphite, a transition from an initial growth of microsized particles to the growth of dendrites with pine tree shape (nanotrees) is observed, which is an advance for materials growth with hierarchical surface roughness. Using kinetic Monte Carlo simulations of an electrodeposition model, those results are explained by the interplay of diffusive cation flux in the electrolyte and relaxation of adsorbed atoms by diffusion on quenched

crystal surfaces. First, simulations on NP patterned substrates show the initial growth of faceted silver particles followed by growth of nanotrees with shapes similar to the experiments. Next, simulations on electrodes with large prebuilt particles explain the preferential nanotree growth at corners and edges as a tip effect. Simulations on wide flat electrodes relate the nanotree width with two model parameters describing surface diffusion of silver atoms: maximal number of random hops (G) and probability of hop per neighbor (P). Finally, simulations with small electrode seeds confirm the transition from initially compact particles to the nucleation of nanotrees and provide estimates of the transition sizes as function of those parameters. The simulated compact and dendritic deposits show dominant (111) surface orientation, as observed in experiments. Extrapolations of simulation results to match microparticle and nanotree sizes lead to $G = 4 \times 10^{11}$ and $P = 0.03$, suggesting to interpret those sizes as diffusion lengths on the growing surfaces and giving diffusion coefficients 2–3 $\times 10^{-13}\mathrm{m}^2/\mathrm{s}$ for deposited silver atoms. These results may motivate studies to relate diffusion coefficients with atomic scale interactions.

Keywords

electrodeposition; silver; thin films; surface diffusion; dendrites; morphological transition

1 Introduction

In recent years, silver deposits with dendritic morphology attracted much attention as catalysts of various reactions[1,2], for their remarkable superhydrofobicity[3], for their antibacterial activity[4], and in other technological applications[2,3,5–9]. The special properties of those structures are related to the high specific surface areas and to the hierarchical organization in treelike or featherlike shapes. Electrodeposition is among the cheapest and most accurate techniques used to grow such nanostructures[10]. The sizes and shapes of the dendrites depend on several microscopic processes, such as ion diffusion in the electrolyte, the electrochemical reactions, and the relaxation of the adsorbed material. These processes are controlled by parameters such as applied current, temperature, pH, and ion concentration is solution. Regulation of deposition conditions may also change the morphology of silver deposits to porous or particulated shapes[5,11,12].

A recent tool to control the morphology of electrodeposited metals is to use patterns of self-assembled gold nanoparticles (NPs) as templates[13]. Their stability is facilitated by coating the NPs with an n-dodecanethiol shell. An advantage of this method is that nucleation occurs in the entire substrate, in contrast with the dominant nucleation at surface defects when the NP pattern is absent[13]. Through appropriate changes of the growth conditions, this approach also allowed tailoring the morphology of the deposits of copper and silver[14,15]. In the case of silver, as the applied potential becomes more negative, a change from faceted microparticles to dendrites is observed; moreover, at high temperatures, plate formation may be observed, which is related to thiol adsorption on the metal surface[15].

Fine tuning of the surface morphology at several length scales is necessary to produce superhydrofobic materials for self-cleaning applications[16–19]. The above electrodeposition method is a prospective route to produce silver materials with that feature if the deposits can mix the microscale roughness of the particles and the nanoscale roughness of the dendrites. In this work, this is achieved with slight changes in the conditions used in previous works. Our study shows evidence of an initial growth of compact, micrometer sized particles, and

a transition to the growth of nanotrees at the corners and edges of those particles. This constitutes a dynamical transition which, to our knowledge, was not formerly reported in those substrates at constant applied potential, and which represents a first step to attain the desired hierarchical structures.

We also perform kinetic Monte Carlo simulations of a properly designed electrodeposition model to relate these results and the microscopic growth mechanisms. The simulations provide a realistic description of the microparticle and dendritic morphologies, reproduce the observed transition, and show the preferential nanotree formation at edges and corners of the particles. Those morphologies are shown to result from the interplay of two key mechanisms: the diffusive cation flux in the electrolyte, which is responsible for shadowing and tip effects, and the surface diffusion of the atoms formed by the electrochemical reaction, which is responsible for shaping the growing crystals. The modeling also advances in the quantitative description of the process, as we argue that the characteristic sizes of the deposited structures are set by the diffusion lengths of silver atoms and we use those lengths to estimate diffusion coefficients. For comparison, although several studies have already highlighted the importance of adsorbate relaxation in the initial stages of metal electrodeposition[20–27] and in the formation of dendritic films[28–32], previous models[32–41] did not show the organized morphology of nanotrees or nanofeathers.

2 Methods

2.1 Experimental Methods

A conventional three-electrode electrochemical configuration is used to perform the electrochemical silver deposition, in which the reference electrode and counter electrode were Ag/AgCl (0.741V vs. normal hydrogen electrode) and a platinum foil, respectively.

A modified (0001) highly oriented pyrolitic graphite (HOPG) substrate is used as a working electrode. It was cleaned by a cleaving process thanks to Scotch tape and, immediately

afterwards, the freshly cleaved (0001) HOPG surface is modified by a droplet of Au NP solution, following similar procedure of recent works[13,15,42].

Functionalized Au NPs with dodecanethiol were synthesized using the method of Stucky[43] and show an average diameter of 4nm with narrow size distribution of about 6%. Au NP functionalization is important because the thiol molecules prevent NP coalescence and act as lubricating agents between the NPs and the HOPG substrate[42,44]. Dodecanethiol was formerly shown to perform better than other ligands to achieve a large scale NP organization[42]. At room temperature, the thiol molecules are mostly at the same plane of the NPs, so the top of the NPs is exposed to the electrolyte.

The Au NP pattern is advantageous for metal electrodeposition because it enables nucleation in the entire substrate, in contrast to the privileged nucleation at defects of the bare HOPG substrate[13], and for the possibility of shaping the silver deposits[15].

A limited area of about 9mm^2 of the substrate is contacted with the electrolyte solution consisting of 10^{-2} M $AgNO_3$ and 1 M $HClO_4$ as supporting electrolyte. The prepared solution was deaerated with purified nitrogen for 2 h before being used for silver electrodeposition. The electrochemical experiments were performed with a Potentiostat/Galvanostat EG/G Model 273A (Princeton Applied Research) at temperature 20°C–21°C and potential −300 mV vs. Ag/AgCl. In these conditions, the thiol molecules are mostly stable at the Au NP plane and, consequently, do not affect the silver electrodeposits; details are discussed in Sec. 3.1.1. Finally, there was no stirring during the electrodeposition.

Silver nitrate, perchloric acid, and dodecanethiol were purchased from Fluka. All chemicals were of analytical grade and were used without further purification. Water purified with the Milli Q system (Millipore, electrical resistivity 18.2 Mcm) was used for all experiments.

The morphologies of the prepared nanomaterials were studied using a LEO 1455 VP high-resolution Field Emission Gun Scanning Electron Microscope (FEGSEM) and a transmission electron microscope (TEM) (JEOL 100CX) operating at 100 kV.

2.2 Electrodeposition Model

The model is defined in a FCC lattice where, for simplicity, the same lattice constant is considered for the deposited material and for the electrodes. A flat electrode is built with (001) orientation at the plane $z = 0$. The other electrodes have seeds with various sizes and shapes adjacent to the plane $z = 0$. The empty sites with $z > 0$ initially contain a supported electrolyte. The size of the simulation cell in x and y directions (lateral size) is denoted as L, with periodic boundaries to avoid size effects.

The incorporation of each atom to the crystal occurs in a sequence of three steps representing the main physico-chemical mechanisms of the process.

First, a cation is released well above the deposit and executes a random walk that ends when it reaches a site with at least one occupied nearest neighbor (NN); Fig. 1(a). This NN may be an atom of the deposit or of the electrode. The random walk represents the diffusive cation motion in an electrolyte with a low concentration in the depleted layer.

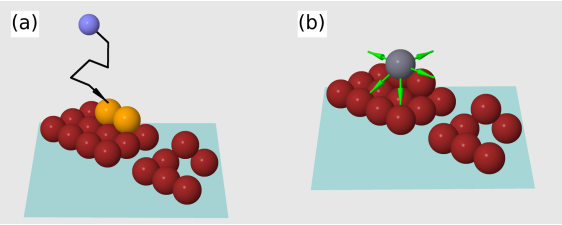

Figure 1: Illustration of the model rules with the substrate $z = 0$ indicated in light blue color and previously aggregated atoms in red or yellow. (a) A cation (blue) in the electrolyte executes the random walk indicated by the arrow and is reduced when it reaches a site with the two highlighted NNs (yellow). (b) Configuration of the deposit after the cation reduction, which forms a mobile atom (gray) at the same position. The acceptable target sites for the first hop of this mobile atom are three positions in the same layer and two positions in the layer below (green arrows).

Second, at the final position of that random walk, the cation is immediately reduced and a mobile silver atom is formed; Fig. 1(b). This step represents an electrochemical reaction whose rate is assumed to be much larger than the rates of mass transport in the solution and on the surface of the deposit.

The third step represents the diffusion of the mobile atom in a quenched configuration

of the crystal surface. Each atom attempts to execute G hops to NN sites and permanently aggregates at its final position. In each hop attempt, a target site is randomly chosen among the NNs of the current position. If the target site is empty and if it has at least one occupied NN, the hop is executed with probability

$$P_{hop} = P^{n-1}, \tag{1}$$

where $P < 1$ and n is the number of occupied NN at the current position (including atoms of the aggregate and of the electrode); if any of those conditions fails, the hop is not executed and the mobile atom remains at its current position. Fig. 1(b) illustrates the acceptable target sites for the first hop of a mobile atom. The condition that the target site of a hop has at least one occupied NN implies that there is no desorption.

This model is an extension of a model previously studied in simple cubic lattices[37,39]. It is designed to represent the main features of the double interface growth mode of silver dendrites, which was shown in transmission electron microscopy (TEM) studies[30,31] and molecular dynamics simulations[45]. A detailed justification is in Sec. SI.I of the Supporting Information.

The hop probability in Eq. (1) implies that the atom mobility is lower (higher) at points with higher (lower) coordination, i.e. sites with higher (lower) bond energy; thus, P is physically expected to increase with the temperature. The number of hop attempts, G, is expected to be proportional to the surface diffusion time of a mobile atom, i.e. the average time in which a deposited atom relaxes while interacting with the crystal surface. A temperature increase leads to the increase of the hopping frequency, so we expect that G increases with the temperature. Moreover, at constant temperature, if the applied current increases, the rate of crystallization increases, which means that each atomic layer of the crystal is formed in a shorter time interval. This implies the decrease of the surface diffusion time, so that G decreases as the applied current increases. Thus, G depends on the interplay

between the temperature and the current, and plays a role equivalent to the diffusion to deposition ratio in models of thin film deposition from vapor[46–48]. However, the quantitative relation between G and those quantities cannot be anticipated because the time interval of surface atom diffusion depends on complex processes occurring from the cation reduction to the atom incorporation to the crystal (Sec. SI.I of the Supporting Information).

The simulation method is presented in Sec. SI.II of the Supporting Information. The unit length in all simulations is half of the lattice constant of silver: $d = 0.204$ nm.

3 Results

3.1 Silver Electrodeposition

3.1.1 The Au NP modified HOPG substrates

To prepare the electrode, the Au NPs were deposited on freshly cleaved HOPG substrate using a drop casting method. The TEM image in Fig. 2 shows that the Au NPs are self-assembled on the HOPG substrate. The two-dimensional hexagonal NP organization is similar to that reported in previous studies[13,15] and is achieved due to their functionalization with dodecanethiol.

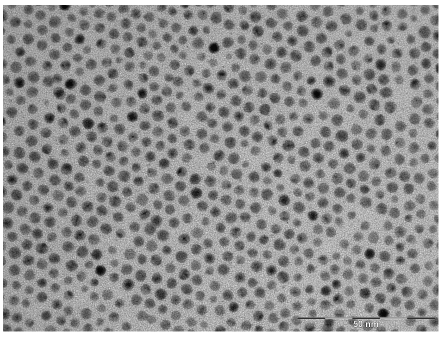

Figure 2: TEM image of Au NPs on the HOPG substrate.

Silver electrodeposition was formerly performed on these substrates using the same electrolyte and the same applied potential, but in different temperatures; that investigation

combined FEGSEM imaging with X-ray diffraction (XRD)[15]. At 62°C, micrometer sized silver platelets with broad (111) facets were obtained because the thiol molecules poison those facets and prevent their growth. As the working temperature is lowered to 38°C, the morphology of the deposits changed to dendritic, with a significant decrease in the (111) XRD peak height; this implies that a much smaller concentration of thiol molecules was bound to the growing silver surfaces. Lowering to 18°C led to a diffraction intensity ratio (111) / (200) similar to that obtained in electrodeposition on bare HOPG electrodes, which indicated negligible effect of the thiol molecules on silver growth; in other words, thiol molecules were not released from the layer of Au NPs that covers the HOPG substrate. Thus, in the temperature range 20°C–21°C of the present work, we can safely assume that the substrate is stable during the electrodeposition process and, consequently, that dodecanethiol molecules do not affect silver growth.

3.1.2 Electrodeposition current

Fig. 3 shows the evolution of the current during the electrodeposition. In the first half of the process, it is near 0.18mA, with a slight trend of increase, but also with some large fluctuations. From ≈ 300 s to ≈ 480 s of deposition, the current decreases to values 0.15–0.16 mA. In the final part of the process, from ≈ 480 s to 600 s of deposition, the current shows a slower time decrease. The current density is in the range 1.7–2.0 mA/cm^2.

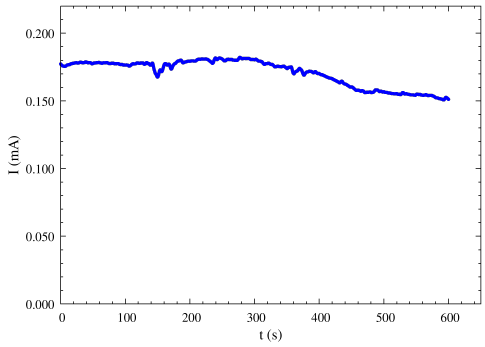

Figure 3: Current as a function of time in the silver electrodeposition. Consecutive points were obtained in intervals of 0.2s.

Fig. 3 does not show two features that are frequently highlighted in potentiostatic works: the current burst associated with nucleation and the subsequent decay associated with formation of a cation depletion layer. The burst is absent due to the progressive nucleation of silver particles during the whole time interval of our experiment, as revealed by images of the deposits (Sec. 3.1.3) and discussed in a previous study of the initial stages of silver electrodeposition on the same substrates[13]. The absence of a current decay can be related to the low cation concentration in the electrolyte. However, if such a decay existed, it would hardly be shown in a plot with time interval of 0.2 s as that of Fig. 3. For comparison, in a recent silver electrodeposition work with much higher ion concentration,[49] current bursts and decays have duration much smaller than 1 s, with current densities in the range 0.5–4 mA/cm^2.

The oscillations in Fig. 3 are also observed in other electrodeposition processes and are related to nucleation and growth of nanoparticles or of grains of polycrystalline films; see Sec. 3.1.3 and Sec. SI.III of the Supporting Information. The oscillations may be related to variations in the surface area available for cation reduction as the nanoparticles or grains nucleate and grow. However, in our experiment, the fluctuations are relatively small, so they are not related to changes in the main physical and chemical mechanisms of the electrodeposition. Indeed, the amplitudes of those fluctuations are mostly below 0.005mA and the largest peak is of 0.01mA, which correspond to 3%–6% of the average measured current in any time interval.

3.1.3 Microparticles and nanotrees

The morphology of the silver deposits is illustrated by the FEGSEM image of Fig. 4(a). Several faceted microparticles are observed, i.e. particles with facet sizes of 1–2μm. Dendrites with the shape of pine trees grow at the microparticle corners and edges. The highlighted region of Fig. 4(a) shows that the nanotrees grown at the particle corners are larger than those grown at the edges, and shows no growth on the flat facets at the FEGSEM resolution.

The higher magnification in Fig. 4(b) confirms the preferential growth of nanotrees at

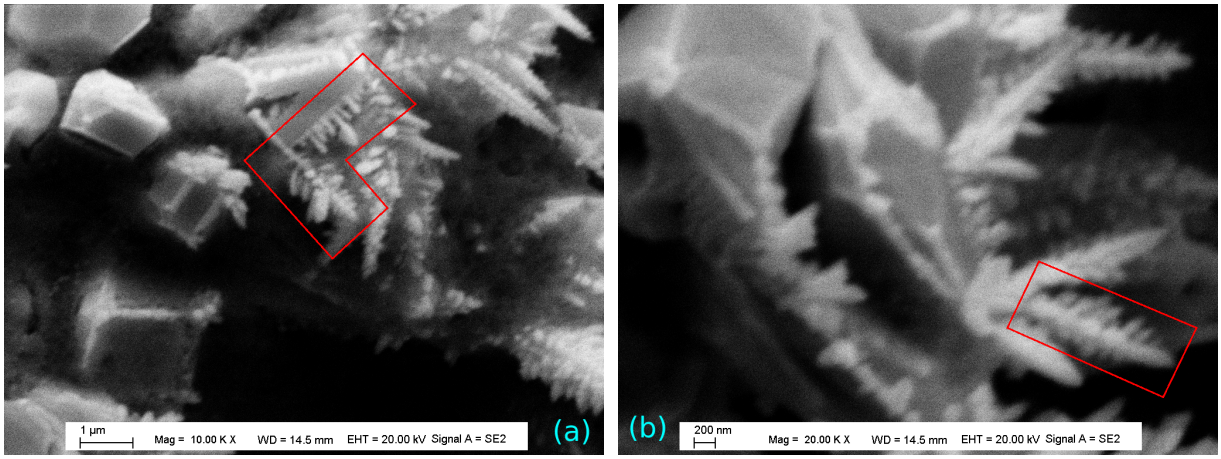

Figure 4: (a),(b): FEGSEM images of the silver electrodeposits after 600s, with different resolutions. The contours in red highlight some dendrites.

the corners and edges. In the highlighted region of Fig. 4(b), a large nanotree has a trunk with width $W_T \sim 200$nm. The distance between the tips of opposite secondary branches is near $W_N \sim 500$nm. These widths provide an approximate value of the dendrite size for application of our model.

In Fig. S1 of the Supporting Information, we show an image of the deposit with lower magnification, which was also obtained after 600s of deposition. The sizes of silver particles range from tenths of micrometers to $> 1\mu$m, while dendrites nucleate and grow at corners and edges [but are less visible than those of Figs. 4(a) and 4(b)]. The large size dispersion of silver particles confirms the progressive nucleation mechanism throughout the 600s of deposition. A comparison with other electrodeposition studies[50,51] supports the interpretation that the current fluctuations in Fig. 3 are associated with the progressive nucleation, which leads to variations in the surface area for cation reduction; see details in Sec. SI.III of the Supporting Information.

The above results are consistent with a transition from an initial regime in which compact silver microparticles are formed to a final regime in which nanotrees are formed. The evolution of the current, shown in Fig. 3, can be related to this transition. In the first half of the process ($\approx$ 0–300 s), the small overall variation of the current is a consequence of the growth of the microparticles: their surface area slowly increases, but the electrical resistance also

does. The decrease of the current in the time interval ≈ 300–480 s is probably associated with the increase in the electrical resistance when the microparticles get thicker. Indeed, note that the current decreases by less than 20% in that interval, so this feature is associated with slow variations in the configuration of the deposit. However, as the nanotrees begin to grow, the current is stabilized because the increase of metal thickness is compensated by the increase of surface area available for cation reduction. Thus, the slow variation of the current from ≈ 480 s to 600 s of electrodeposition (Fig. 3) can be associated with the nanotree growth.

Silver electrodeposition on the same substrates was previously performed under almost the same conditions adopted here[15], but at a slightly lower temperature of 18°C. Much larger silver dendrites were grown, with trunks reaching some tens of micrometers, but the formation of microparticles in the beginning of the process was not reported. With a lower potential of −100mV, the same electrolyte, and the same temperature, faceted microsized Ag particles were formed, but no dendrite. Thus, the main advance of our experimental study is to show evidence that the morphological transition (from microparticles to nanotrees) occurs during the electrodeposition without changes in the applied potential or in other physical or chemical parameters.

Using X-ray diffraction, it was formerly shown that the (111) crystallographic planes are dominant in the compact and in the dendritic morphologies[15]. In the present experiment, Figs. 4(a)-(b) show that the corners of microparticles are intersections of three facets, which is a signature of the (111) orientation of those facets.

3.2 Simulations of Electrodeposition on Nanoparticle Patterned Substrates

The simulation study begins with deposition on substrates containing hemispherical NP patterns shown in Fig. 5(a). Cation reduction is allowed at the surfaces of the NP seeds (which represent the gold NPs of the experiments), and in contact with the deposited material

(which represents silver), but is not allowed in contact with the underlying substrate. That substrate is a square lattice and the NP pattern follows this geometry.

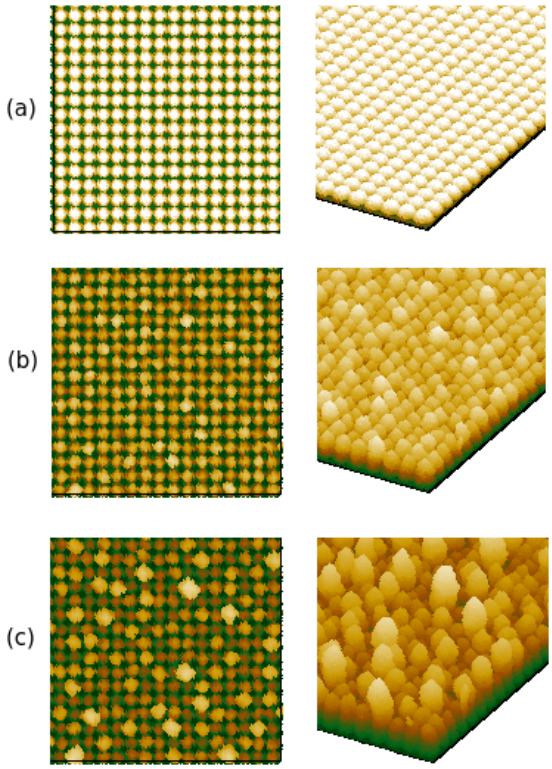

Figure 5: Top and perspective views of: (a) substrate with a pattern of hemispherical NP seeds; (b) part of a deposit produced with $G = 10^4$ and $P = 0.1$ at dimensionless time $T = 5$; (c) part of the same deposit at $T = 10$. In the top views, [100] and [010] directions are horizontal and vertical, respectively. The colors in each panel vary from black (smallest height) to white (largest height), so the color-height relation is different in different panels.

Figs. 5(b) and 5(c) show top and perspective views of parts of the deposits obtained at short times with $G = 10^4$ and $P = 0.1$. Several compact particles grow on the top of the initial NPs, but many NPs are covered only by narrow deposited layers, as revealed by the darkest colors' contrast in Fig. 5(c). The perspective views show that the largest deposited particles have pyramidal shape with a vertically oriented apex ([001] direction), while the top views show that the pyramid facets are oriented at 45° with [100] and [010] directions. This indicates a dominant (111) orientation of the facets, which is the lowest energy planar configuration, consistently with the relaxation mechanism of mobile atoms.

The top view of Fig. 5(c) shows the increase in the size of the largest particles, while a

large number of small particles are also present. This implies a large dispersion in the sizes of the deposited particles; the largest widths are near 20 simulation units, while the smallest widths are below 10, which is near the distance between neighboring NPs. This large size dispersion and the dominant (111) orientation agree with the experiments.

Figs. 6(a) and 6(b) show top and perspective views of the deposits grown with the same parameters at longer times. Now we observe the growth of self-organized structures (dendrites) with the shape of pine trees, which are similar to those of the experiments [Figs. 4(a)-(b)]. Thus, the electrodeposition model shows the same morphological transition from compact particles to dendrites with nanotree shape. The trunks of the nanotrees grow in the [001] direction and the top views of Figs. 6(a)-(b) show that the secondary branches grow in directions $[\pm 1, 0, 0]$ and $[0, \pm 1, 0]$.

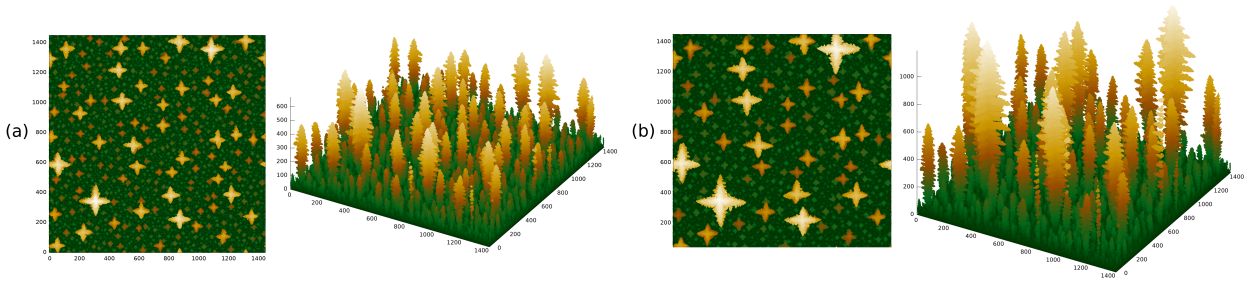

Figure 6: Top and perspective views of a deposit produced with $G = 10^4$ and $P = 0.1$ at dimensionless times (a) $T = 40$ and (b) $T = 56$. The colors in each panel vary from black (smallest height) to white (largest height), so the color-height relation is different in different panels. All lengths are given in simulation units.

The sizes of deposited particles in these simulations are much smaller than the nanotree widths, which quantitatively differs from the experiments. However, these simulations are performed at nanoscale, where all characteristic sizes are much smaller than those of the experiments. The quantitative application of the model with the experimental sizes (Sec. 4.1) gives a value of G much larger than those accessible to direct simulations.

3.3 Simulations of Electrodeposition on Large Particles

Here we perform simulations in electrodes with large prebuilt particles, i.e. the growth of these particles is not simulated. The electrodes are formed by these particles and the plane $z = 0$, so cations can also be reduced on that plane.

Fig. 7(a) shows snapshots of the deposit when the particle has the shape of a truncated pyramid, whose top is a (001) plane and whose sides are $(\pm 1, \pm 1, 1)$ planes. At short times, some trees preferentially grow at the corners of the pyramid, smaller trees nucleate at the edges, and small islands are formed at the top of the particle and at the bottom plane. At the longest time, these islands give rise to small trees, but the trees at the corners and edges advance faster. The growth is dominated by the four largest nanotrees at the corners, which have secondary and tertiary branches.

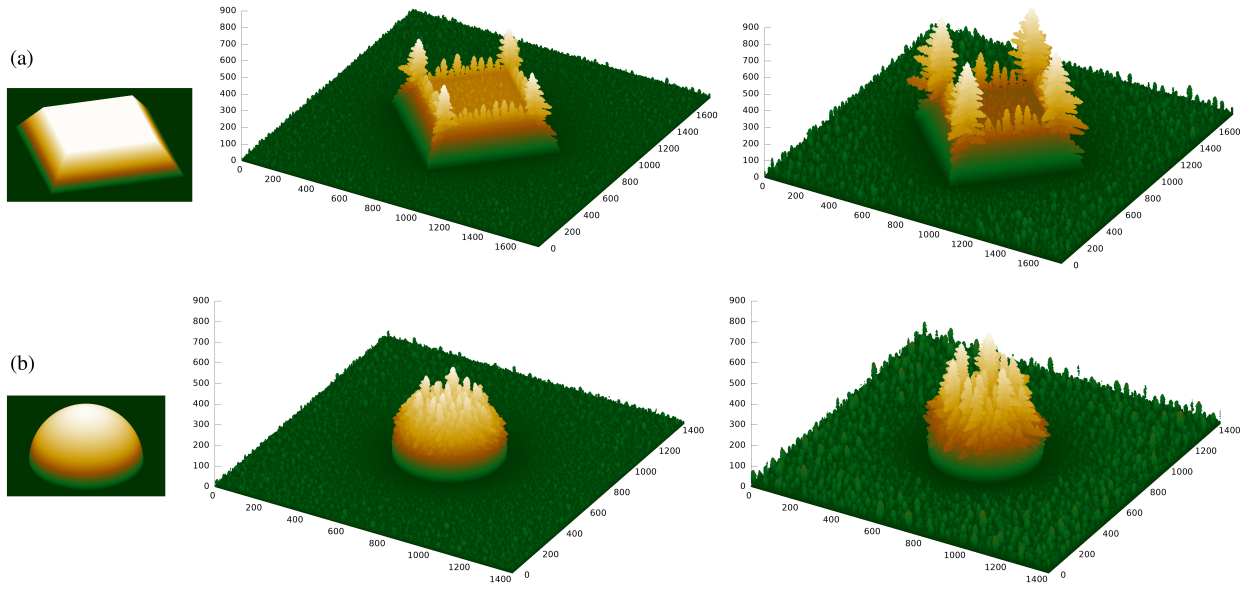

Figure 7: Snaphots of deposits for $G = 10^4$ and $P = 0.1$ on (a) a pyramidal particle and (b) a hemispherical particle, with increasing deposition time from left to right. The color scheme (from dark green to white) is associated to the range of z of each image, so a color may correspond to different z in different images. All lengths are given in simulation units.

Fig. 7(b) shows snapshots of the deposits formed with a hemispherical particle, for the same growth parameters and the same amount of deposited material of Fig. 7(a). The largest aggregates initially grow on the topmost parts of the particle and the smallest aggregates

grow on the plane $z = 0$. As the deposition continues, the nanotrees on the top of the particle grow faster than those at other points.

We also observe a similarity between the morphologies of the nanotrees obtained in these simulations and in the experiments. The nanotrees preferentially grow on the particle surfaces instead of the plane $z = 0$ due to a shadowing effect of the most protuding parts of the electrode, i.e. most of the randomly moving cations reach the particles before reaching the plane $z = 0$. This shadowing is confirmed by the absence of growth near the intersections between the particles and that plane.

The preferential growth at corners and edges of the pyramidal particle is also consistent with the experimental observations, but it is not observed in the hemispherical particle because it is a tip effect. The stationary cation concentration in the electrolyte is described by the Laplace equation, so the highest concentration gradients occur near the edges and corners of the boundary surface. This leads to larger cation currents in those regions, so reduction is more likely to occur there. As the nanotrees get taller, the tip effect is enhanced. This interpretation is consistent with the recent observation of a concentration gradient in the solution near silver dendritic particles synthesized by galvanic replacement reaction [52].

The results of this section and of the previous one show that the model represents the main physical and chemical mechanisms of the silver electrodeposition. The shadowing and the tip effects show that the deposition flux is dominant over the energetics at large length scales. Indeed, at corners and edges, a mobile atom has 1 to 3 NNs, so those positions are energetically unfavorable in comparison with sites of the pyramid facets, which have 3 or 4 NNs. However, the energetics is dominant at short scales because the adatom diffusion is responsible for shaping the compact particles and the nanotrees. Indeed, a model without diffusion would be equivalent to diffusion limited deposition (DLD), which produces deposits with randomly growing branches [53], a morphology very different from the nanotrees.

3.4 Simulations of Electrodeposition on a Flat Electrode

A flat electrode allows the growth of many dendrites in a single simulation, with size dispersion smaller than that of Figs. 6(a)-(b), but restricted to small G due to computational limitations. The average dendrite width is then measured with higher accuracy.

3.4.1 Nanotree Morphology

Figs. 8(a)-(f) show images of the deposits obtained with an electrode at $z = 0$, for $P = 0.1$ and several G; from top to bottom, a perspective view, a top view, and a lateral view are presented.

The model with $G = 0$ (no hop of the adsorbed atoms) is equivalent to DLD, which produces highly branched deposits with fractal properties, but without self-organization [53,54]. For $G \lesssim 10^3$ (small numbers of hop attempts), Figs. 8(a)-(b) also show that aggregates with random ramification predominantly grow, similarly to DLD.

For $G \gtrsim 10^4$ [Figs. 8(d)-(f)], the growth of nanotrees is observed, which are also similar to the silver nanotrees in Figs. 4(a)-(b). Close inspection of the lateral views shows tertiary branches growing in [001] and $\left[00\overline{1}\right]$ directions. Note that the $\left[00\overline{1}\right]$ branches are shadowed by the secondary branches, so their formation is evidence of the effects of surface diffusion. This result confirms the interpretation that the short scale features of the nanotrees are controlled by the energetics.

Figs. 9(a)-(b) show snapshots of the initial growth of a nanotree. The trunk begins as a truncated pyramid with lateral facets in $(\pm 1, \pm 1, 1)$ orientation, but with (001) terraces at the top. The faster propagation of the lateral edges leads to nucleation of secondary branches. As the secondary branches increase, they show the same truncated pyramid shape of the trunk [Fig.9(b)], but propagate in perpendicular directions.

For these reasons, most of the nanotree surface area, which consists of trunk sides and branch sides, has (111) orientation. This result is consistent with the dominant (111) orientation obtained in experiments [15].

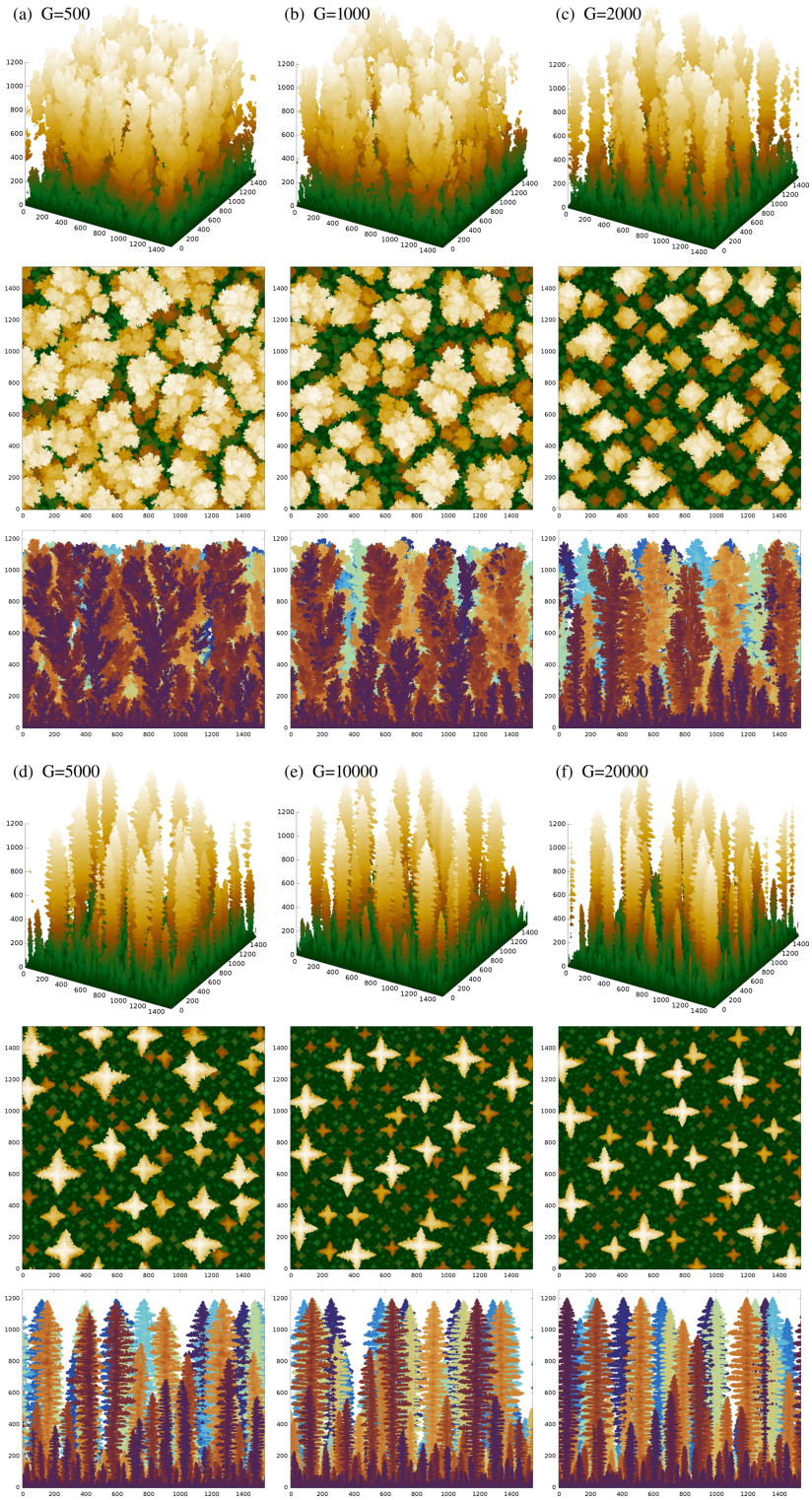

Figure 8: Images of simulated deposits with $P = 0.1$ and: (a) $G = 5 \times 10^2$; (b) $G = 10^3$; (c) $G = 2 \times 10^3$; (d) $G = 5 \times 10^3$; (e) $G = 10^4$; (f) $G = 2 \times 10^4$.

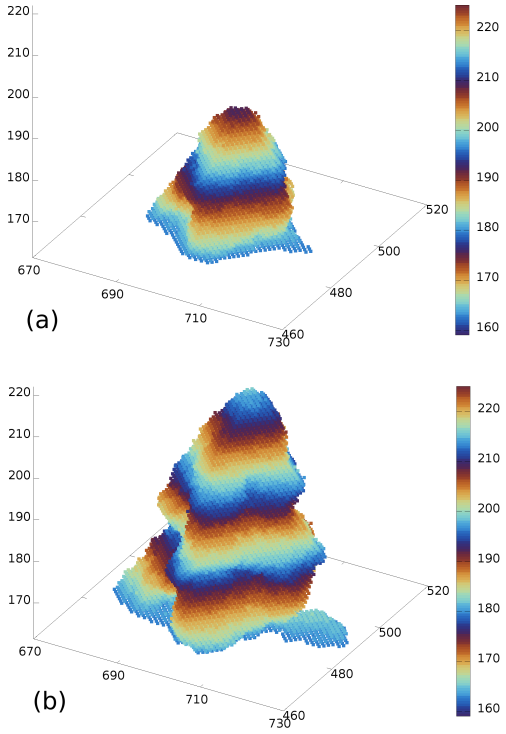

Figure 9: Snapshots of the initial growth of a nanotree, with dimensionless simulation times (a) $T = 800$ and (b) $T = 1790$. Model parameters are $G = 10^4$ and $P = 0.1$.

3.4.2 Nanotree width

The average width W of the nanotrees is calculated with a method similar to previous works[39]; see Sec. SI.IV of the Supporting Information. The main contributions to W come from the trunk width, from the widths of the secondary branches, and from the distances between opposite secondary tips.

Fig. 10 shows W as a function of GP^3, which provides an excellent data collapse for several model parameters. For $GP^3 \gtrsim 10$, the linear fit in Fig. 10 gives

$$W \approx 3.6\big(GP^3\big)^{0.39}, \tag{2}$$

with W in simulation units. Eq. (2) implies that W is more strongly affected by changes in P than by changes in G; this is visually confirmed in Fig. S3 of Sec. SI.V of the Supporting Information.

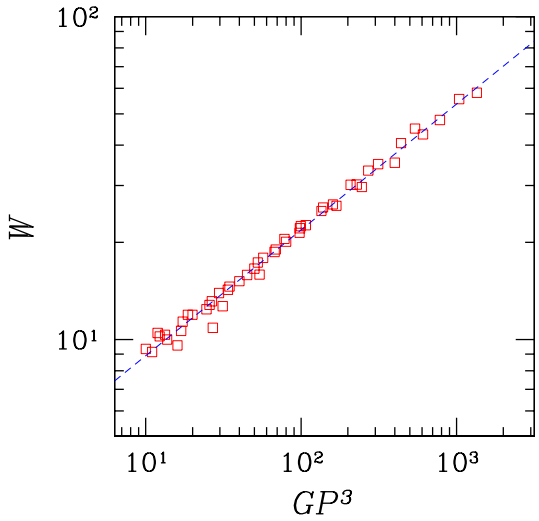

Figure 10: Average dendrite width W as a function of the scaling variable GP^3. The plotted data have $2 \times 10^3 \leq G \leq 5 \times 10^4$ and $0.06 \leq P \leq 0.3$. A linear fit of the data with $GP^3 > 10$ (dashed blue line) is shown.

The factor P^3 is the hopping probability of a mobile atom on a (001) terrace [Eq. (1)], where it has $n = 4$ NNs [for an illustration, see Fig. S4(a) of Sec. SI.VI of the Supporting Information]. Only 1/3 of the hop attempts are accepted on a wide (001) terrace, from a total of G attempts, so the average number of executed hops on this terrace is $GP^3/3$. Thus, Eq. (2) indicates that atom diffusion on the (001) terraces of the dendrite tips [Figs. 9(a)-(b)] is the mechanism that controls the dendrite width.

Previous simulations of the same model in simple cubic lattices produced maple leaf dendrites with tips formed by (001), $(\pm 1, 0, 0)$, and $(0, \pm 1, 0)$ terraces[39], on which the average number of hops of an atom is G. The cross sectional area of the dendrites scaled approximately as $G^{0.8}$, so the average width scaled as $G^{0.4}$, a relation with an exponent similar to that of Eq. (2). This provides quantitative support to the interpretation that the diffusion on the nanotree tips controls the nanotree growth. The exponents ≈ 0.4 are smaller than the free random walk exponent 0.5 on a wide surface due to the irregular landscape of the dendrite tips.

3.5 Simulations of the Transition from Particles to Nanotrees

Here we simulate the electrodeposition on a single small seed with approximately cubic shape placed on an inert plane $z = 0$ (i.e. cations can be reduced only in contact with the seed). This allows simulations with much larger G to estimate the transition sizes from particles to nanotrees.

3.5.1 Morphology in the Transition

Figs. 11(a) and 11(b) show snapshots of the deposits produced with different parameter sets. At short deposition times, compact particles with pyramidal shape are formed with facets mostly in (111) orientation. The bottom plane with (001) orientation does not affect this result. After some time, the pyramids are deformed because their edges grow faster than the facets. Fig. S5 of Sec. SI.VII of the Supporting Information shows top views which also illustrate these deformations.

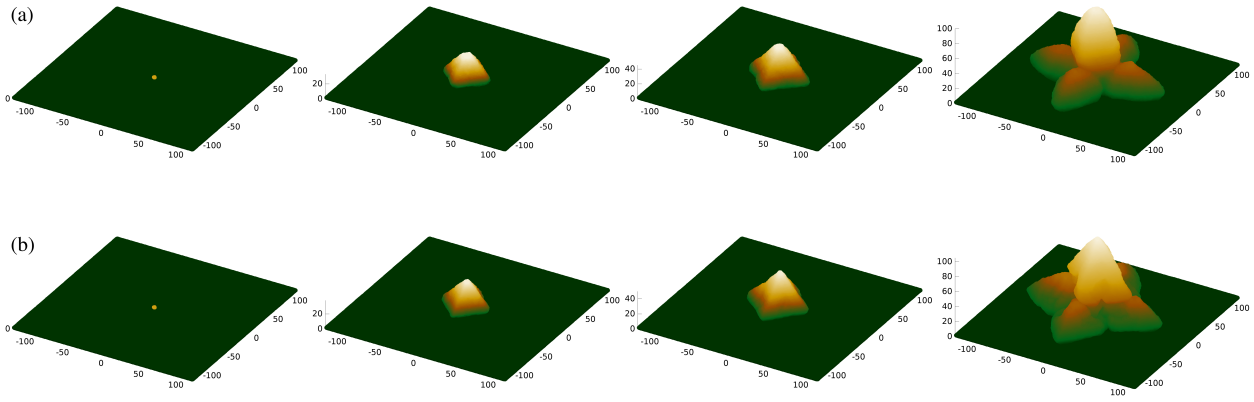

Figure 11: Images of the simulated deposits with a small seed. (a) $G = 5 \times 10^4$, $P = 0.2$: from left to right, dimensionless times are $T = 0$, 37, 78, and 500. (b) $G = 10^6$, $P = 0.05$: from left to right, $T = 0$, 80, 162, and 10800. All lengths are in simulation units.

At the longest times, the deposited material spreads with a star-like shape. The central part of the deposit gives rise to a dendrite trunk that grows in the $+z$ direction. The protuberances of the trunk in $\pm x$ and $\pm y$ directions indicate the nucleation of secondary

branches; for instance, compare the images in Figs. 11(a) and 11(b) with those in Figs. 9(a) and 9(b).

These simulations show a morphological transition equivalent to the experiments. The particle facets have the same (111) orientation of the experiments, despite the choice of the (001) orientation for the bottom surface. This reinforces the interpretation that the energetics is responsible for the short length scale features. However, as those particles become large, the competition between the growth kinetics (diffusive cation flux in the electrolyte) and the energetics (surface diffusion of atoms) begins to play a role. The formation of a branched morphology is a consequence of that kinetics.

Note that the growth of initial faceted particles was possible because we considered large values of G. For instance, for $G = 10^4$ and $P = 0.1$, Fig. S6 of Sec. SI.VII of the Supporting Information shows that a nanotree begins to grow relatively early, preventing an accurate estimation of the sizes of initial compact structures.

3.5.2 Transition Size

We measured two average lengths at the lowest z plane of the deposits to characterize the compact particles: a diagonal length l_d, which is calculated in the $[1, 0, 0]$ and $[0, 1, 0]$ directions, and a side length l_s, which is calculated in the $[\pm 1, \pm 1, 0]$ directions. The transition length S_t is defined as the value of l_s in which $l_d/l_s = \sqrt{2}$ because this is the aspect ratio of base lengths in a perfect pyramid with lateral $(\pm 1, \pm 1, 1)$ facets. For instance, for $G = 10^6$ and $P = 0.05$, this method gives $S_t \approx 78$ at the dimensionless growth time $T = 167$, which is near the time of third panel of Fig. 11(b), where a small deformation of the pyramidal shape is observed. Details of the calculation of S_t are in Sec. SI.VIII of the Supporting Information.

Fig. 12 shows S_t as a function of G for several $P \leq 0.1$. For constant P, S_t varies as a power law of G; however, the power laws have exponents varying from ≈ 0.25 for $P = 0.1$ to ≈ 0.45 for $P = 0.01$. Thus, contrary to the dendrite width, we cannot express S_t as a single

power law of G and P.

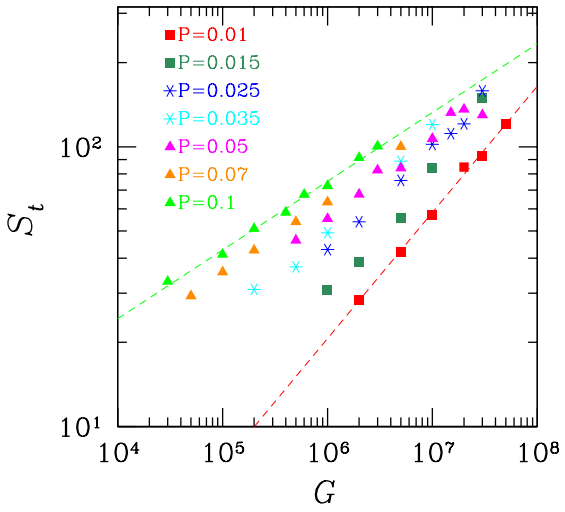

Figure 12: Transition size as a function of G. Dashed lines show linear fits of the data with $P = 0.01$ and $P = 0.1$. All lengths are given in simulation units (half of the lattice constant).

To relate S_t with both parameters, we first performed linear fits of the $\log S_t \times \log G$ plots for constant P, as illustrated in Fig. 12 for $P = 0.01$ and $P = 0.1$. Next we obtained the P-dependence of the slopes and intercepts of those fits; see details in Sec. SI.IX of the Supporting Information. For $0.01 \leq P \leq 0.05$, this leads to the approximate relation

$$\log_{10} S_t \approx (0.51 - 4.7\ P) \log_{10} G + 39\ P - 1.8, \tag{3}$$

where S_t is given in simulation units. The coefficients in Eq. (3) have uncertaities $\sim 10\%$.

4 Discussion

4.1 Application of the Model to the Silver Electrodeposition

The present study of silver electrodeposition shows for the first time a transition from a compact to a dendritic morphology during the growth on Au NP modified HOPG substrates. Such changes were formerly observed only if the growth parameters (e.g. applied potential

or temperature) were changed[15]. This advance permits to calibrate the parameters of the model, which may be helpful for further experiments and applications of these materials.

The experiments show microparticles with facets of maximal sizes $S_{exp} \sim 1\mu$m and dendrite growth on them. We understand that S_{exp} is an estimate of the transition size. Considering the length unit in the simulations $d = 0.204$ nm, it gives $S_t = S_{exp}/d \sim 5 \times 10^3$ in simulation units. Using Eq. (3), this provides a numerical relation between G and P.

The dendrite width in the experiments is estimated as the average between the trunk width $W_T \approx 200$nm and the nanotree width $W_N \approx 500$nm (Sec. 3.1): $W_{exp} \approx 350$nm. This method parallels the approach used in the simulations (Sec. SI.IV of the Supporting Information). That value corresponds to $W = W_{exp}/d \approx 1.7 \times 10^3$ in simulation units. Using Eq. (2), we obtain a second numerical relation between G and P.

The solution to the two relations between G and P is

$$G = 4 \times 10^{11} \quad , \quad P = 0.03 \quad . \tag{4}$$

Here the values have only one significant figure due to the low accuracy of the experimental data and the uncertainties in Eqs. (2) and (3). The value of P is within the range of our simulations, but the value of G is too large for our current computational capability; observe that the values of S_t and W exceed the size of our simulation cell. However, the extrapolation of Eqs. (2) and (3) is reliable in view of the thorough estimation of those scaling laws for broad ranges of parameters.

These estimates also explain apparent discrepancies between simulation and experimental sizes. In the FEGSEM images of Figs. 4(a)-(b), the facet sizes of silver microparticles are larger than the nanotree widths, which are respectively of orders 1μm and 0.1μm. Instead, in the simulations of Figs. 11(a)-(b), the pyramidal particles have sizes ~ 10 nm, but the nanotree width is slightly larger. This occurs because S_t and W have very different relations with G and P [Eqs. (2) and (3)].

4.2 Diffusion Lengths of Silver Atoms

According to the model definition (Sec. 2.2), a mobile atom chooses one NN for any hop attempt (from a total of 12 NN) and the hop is accepted only if that NN has at least one occupied NN. If the atom is on a (111) terrace, the hops to 6 NN can be accepted, which are the NN in the same (111) plane. If the atom in on a (001) terrace, the hops to 4 NN can be accepted. For illustrations, see Figs. S4(a)-(b) of Sec. SI.VI of the Supporting Information.

Now consider a mobile atom on a wide (111) terrace, which is dominant in the microparticle facets. Since each hop has probability P^2, the average number of executed hops is $6GP^2/12 = GP^2/2$. The corresponding diffusion length (root mean square displacement) of a free atom on this terrace is $r_{111} \approx \sqrt{GP^2/2}\sqrt{2}d$, where $\sqrt{2}d$ is the distance between NNs. Using the parameters in Eq. (4), we obtain $r_{111} \approx 4\mu$m. This length is 4 times larger than the size of the microparticle facets in the experiments, $S_{exp} \sim 1\mu$m. This is reasonable because those facets are expected to have many atoms and islands, so the silver atoms cannot reach the same distance of an atom on a perfectly flat (111) terrace.

If a mobile atom is on a wide (001) terrace, the extension of the above arguments leads to the diffusion length $r_{001} \approx \sqrt{GP^3/3}\sqrt{2}d \approx 0.6\mu$m for free atoms. This value is larger than the widths of the nanotree trunks, $W_T \approx 200$ nm. This is also consistent because the tips of those trunks are not perfect (001) terraces, so the silver atoms cannot reach the same distance of an atom on a perfectly flat (001) terrace.

Although r_{111} and r_{001} exceed the sizes S_{exp} and W_T, respectively, they differ by small factors $\approx$ 3–4. Thus, we understand that S_{exp} and W_T can be used to estimate the actual diffusion lengths of silver atoms on their growth fronts. The layer by layer growth of the microparticle facets is possible if the deposited atoms spread through a length of the order of half of their size, i.e. if the atoms deposited at the facet border can reach the center of the facet and vice-versa; this gives a diffusion length $l_m \approx S_{exp}/2 \approx 500$nm on the microparticle facets. This value is consistently smaller than r_{111} (which would be applicable to perfectly flat surfaces). For the same reason, the average diffusion length of an atom on the tips of

the nanotrees is expected to be $l_n \approx W_T/2 \approx 100$nm; this is also consistently smaller than r_{001}.

4.3 Diffusion Coefficients of Silver Atoms

Our first step is to estimate the average times of diffusion of silver atoms on the surfaces of microparticles and nanotrees. The motion of an atom begins when it arrives at a close neighborhood of the crystal surface and ends when it permanently aggregates to the crystal. Here we assume that the atom is mobile during the time interval in which an atomic layer of the crystal is formed: τ_m on microparticle facets, τ_n on nanotree trunks. This kinetic hypothesis is frequently used in the interpretation of results of deposition models[48,55].

From the current evolution (Fig. 3), we estimated that the nanotrees are mostly formed from 480 s to 600 s of electrodeposition, so a rough estimate of the growth time of the largest nanotrees is $t_n \sim 10^2$ s. Most of the electrodeposition time is associated to the microparticle growth, so a rough estimate is $t_m \sim 5 \times 10^2$ s.

The microparticles in Figs. 4(a)-(b) have facets of size $S_{exp} \sim 1\mu$m, so their atomic layers are piled up to the thickness $S_{exp}/2 \sim 500$ nm in the time interval t_m. The distance between atomic layers in the [111] direction is $d_{111} = 0.236$ nm, so the average time for formation of an atomic layer is $\tau_m = t_m d_{111}/\left(S_{exp}/2\right) \sim 0.2$ s. The diffusion coefficient of a silver atom on the microparticle facet is

$$D_m \sim \frac{{l_m}^2}{4\tau_m} \sim 3 \times 10^{-13} \text{ m}^2/\text{s}. \tag{5}$$

The tallest nanotree highlighted in Fig. 4(a) has height $H \approx 1.5$ μm and grew in the time interval t_n. The distance between two atomic layers of silver in the [001] direction is $d_{001} = 0.204$ nm, so the average time for growth of an atomic layer of the trunk is

$\tau_n = t_n\ d_{001}/H \sim 10^{-2}$ s. The diffusion coefficient of an atom on the nanotree tip is

$$D_n \sim \frac{{l_n}^2}{4\tau_n} \sim 2 \times 10^{-13}\ \mathrm{m}^2/\mathrm{s}. \tag{6}$$

These estimates indicate that the transition from a compact particle morphology to a dendritic structure is not accompanied by a significant change of the silver diffusion coefficient on the growth fronts. As reviewed in Sec. SI.I of the Supporting Information, the growth of the silver dendrites occurs via the incorporation of atoms from an amorphous layer that surrounds the crystal, while the cation reduction takes place at the interface between that amorphous layer and the electrolyte[30,45]. Thus, D_m and D_n describe the effective diffusion of atoms of those amorphous layers near the crystal surfaces. Their similar values indicate that the dominant orientations of these surfaces weakly affect (if affect) those coefficients.

4.4 Comparison with Results of Other Studies

To the best of our knowledge, no previous work has obtained an estimate of the diffusion coefficient of silver atoms on the surface of an electrodeposited dendrite. Thus, here we can only make comparisons with surface diffusion coefficients in other conditions.

Recent studies have shown the importance of nanocluster diffusion in the initial stages of electrodeposition of metals such as Ag and Pt on weakly interacting substrates[25]. A numerical model developed for silver electrodeposition on carbon and ITO substrates considers diffusion coefficients 10^{-9}–$10^{-8}\mathrm{m}^2/\mathrm{s}$ for single atoms.[56] The interactions of Ag atoms with such substrates are expected to be much weaker than those with a crystalline Ag surface, so it is physically reasonable that those values are much larger than the estimates of Eqs. (5) and (6).

We may also compare the estimated coefficients with those of silver atom diffusion on Ag planes during vapor deposition. For atoms on Ag(001) terraces, the island densities obtained in a broad range of temperatures T give the diffusion coefficient[57,58] $D_{V,001} =$

$1/4\left(\sqrt{2}d\right)^2 \nu \exp\left[-E_d/\left(k_B T\right)\right]$, where $\nu \approx 10^{13}\mathrm{s}^{-1}$ and $E_D = 0.38\mathrm{eV}$. At 20°C, in which our experiments were performed, this relation gives $D_{V,001} = 6 \times 10^{-14}\mathrm{m}^2/\mathrm{s}$. On Ag(111) terraces, the same form of the diffusion coefficient is applicable with $\nu \approx 2 \times 10^{11}\mathrm{s}^{-1}$ and $E_D = 0.097\mathrm{eV}$[58,59], i.e. with a much smaller activation energy. At 20°C, it gives $D_{V,111} \approx 1 \times 10^{-10}\mathrm{m}^2/\mathrm{s}$.

Thus, in high vacuum conditions, the diffusion coefficient of silver atoms in (111) terraces is more than three orders of magnitude larger than the coefficient in (001) terraces. This constrasts with the small difference between D_m and D_n, although these coefficients were also obtained in regions where the dominant crystal orientations were (111) and (001), respectively. The comparison suggests that features other than the crystal orientation are more important to determine the surface diffusion coefficients of atoms during silver electrodeposition.

4.5 Comparison with Other Dendrite Shapes

A recent work showed electrochemically grown silver dendrites similar to those obtained here, in which branches grow perpendicular to a trunk[9]. This was achieved with low concentrations of silver ions in the electrolyte and in a case of very high applied potential. The results have a parallel with those presented here because we also used low concentrations in the electrolyte.

However, silver dendrites produced in several electrodeposition studies have feather-like shape[3,8,60,61]. As shown in scanning electron micrographs by Radmilovic et al[61], these dendrites are two-dimensional (2D) structures whose trunks and branches propagate in [112] directions[61], but their surfaces mostly have (111) orientation. This morphology is very different from the pine trees obtained here, which symmetrically spread in three dimensions (3D), with [001] propagation favored by the substrate orientation.

To check whether this difference is related to the substrate orientation, we simulated the model using a substrate with normal direction [112]; see Sec. SI.X of the Supporting Information. However, the dendrites did not grow in the [112] direction and the secondary

and tertiary branches spread in 3D. The growth is slower in the branches that are partly oriented in the $[\overline{112}]$ direction, which may be ascribed to the orientation of the cation flux.

In electrodeposition, we understand that dendrites result from an interplay of cation flux, cation reduction, and adsorbed atom diffusion (the latter being related to the energetics of the metal surface). Thus, the formation of the 2D dendrites must be associated to some symmetry in these mechanisms, which is not captured in the present model. However, the search for such a symmetry is out of the scope of the present work.

5 Conclusion

We performed parallel experimental and computational studies to explain the observed morphological changes of silver electrodeposits on Au NP modified HOPG substrates, which has recently emerged as a versatile tool for metal electrodeposition.

The experiments were perfomed in conditions close to those of previous works that showed the formation of dendritic structures[15]. However, FEGSEM images reveal the initial formation of microsized particles followed by the growth of nanotrees at their corners and edges, which is a dynamic transition not previously reported in those substrates. Note that other electrodeposition approaches regulated the morphologies of silver deposits by changing the conditions of operation, but they did not show the transition observed here in a single electrodeposition experiment[5,11,12]. Thus, understanding the transition showed in this work is essential to improve the method for the production of the morphologies of interest for each application.

We propose a model for silver electrodeposition that assumes diffusive cation flux in the electrolyte and surface relaxation of the adsorbed atoms by diffusion on quenched configurations of the growing crystal. Simulations of the model are performed on electrodes with several shapes. Considering plane electrodes patterned with nanoparticle seeds, we show the formation of initially compact particles followed by the growth of nanotrees, in qualitative

agreement with the transition of the experiments. Using electrodes with large preformed particles, we relate the preferential growth of nanotrees at corners and edges to a tip effect due to the diffusive cation flux. Similar nanotrees grow on initially wide and flat deposits, confirming that the large scale morphology is controlled by the flux kinetics, while the short lengthscale features of the nanotrees are determined by the energetics (via the surface diffusion of adsorbed atoms). This interpretation is confirmed in the simulations with small electrode seeds, which also show the transition from initially compact (pyramidal) particles to the nucleation of nanotrees. The surfaces of particles and dendrites mostly have (111) orientation, which is also in agreement with experimental observations (the only exception are the (001) terraces at the nanotree tips).

Using typical values of microparticle facet size and of nanotree width of the experiments, and extrapolating the scaling relations of these lengths from the simulations, the two model parameters that reproduce the experimental data are determined. We argue that the microparticle and nanotree sizes provide estimates of the diffusion lengths of the atoms deposited on their growth fronts. This allows the estimation of diffusion coefficients of silver atoms, which are of order $\sim 10^{-13}\mathrm{m}^2/\mathrm{s}$, independently of the dominant orientation [(001) or (111)] of the growth front. To our knowledge, this is the first estimate of these coefficients in silver electrodeposition, which may motivate ab initio approaches or molecular dynamics studies for a comparison.

Observe that a morphological transition was also recently observed in a study of cobalt electrodeposition[23], in which SEM images showed the initial growth of hexagonal nanoplatelets followed by the growth of nanoflakes. The surface diffusion of cobalt nanoclusters was highlighted as an important ingredient of that process. However, the nanoflakes did not grow only on the nanoplatelet surfaces, but also on the electrode, and were associated with the precipitation of cobalt hydroxide; these features are significantly different from those shown in the present work. Despite these differences, we expect that the quantitative modeling introduced here may help to control the growth of hierarchical silver nanostructures in other

conditions and may be extended to electrodeposition of other metals. The modeling can also include dissolution mechanisms (e.g. those used to describe dealloying[62]) to study reversible electrodeposition[63–65], which may help to find the best conditions for dendrite elimination.

Supporting Information Available

The Supporting Information file contains a justification of the model, details of the simulation method, additional FEGSEM images, additional images of simulated deposits (various conditions), details of the calculation of the average width of nanotrees, and detais of the method to determine the transition size as a function of the model parameters.

Acknowledgment

F.D.A. Aarão Reis acknowledges support from the Brazilian agencies Faperj (E-26/202.881/2018, E-26/210.354/2018), CAPES (88887.310427/2018-00), and CNPq (305391/2018-6).

References

(1) Cheng, Z.-Q.; Li, Z.-W.; Xu, J.-H.; Yao, R.; Li, Z.-L.; Liang, S.; Cheng, G.-L.; Zhou, Y.-H.; Luo, X.; Zhong, J. Morphology-Controlled Fabrication of Large-Scale Dendritic Silver Nanostructures for Catalysis and SERS Applications. Nanoscale Res. Lett. **2019**, 14, 89.

(2) Raj, A. K.; Murugan, C.; Rameshkumar, P.; Pandikumar, A. Growth of Silver Nanodendrites on Titania Nanotubes Array for Photoanode Driven Photoelectrocatalytic Reduction of Carbon Dioxide. Appl. Surf. Sci. Adv. **2020**, 2, 100035.

(3) Xu, X.; Zhang, Z.; Yang, J. Fabrication of Biomimetic Superhydrophobic Surface on

Engineering Materials by a Simple Electroless Galvanic Deposition Method. Langmuir **2010**, 26, 3654–3658.

(4) Pal, S.; Tak, Y. K.; Song, J. M. Does the Antibacterial Activity of Silver Nanoparticles Depend on the Shape of the Nanoparticle? A Study of the Gram-Negative Bacterium Escherichia coli. Appl. Environ. Microbiol. **2007**, 73, 1712–1720.

(5) Liu, W.; Yang, T.; Li, C.; Che, P.; Han, Y. Regulating Silver Morphology via Electrochemical Reaction. CrystEngComm **2015**, 17, 6014–6022.

(6) Cho, Y.-B.; Moon, S.; Lee, C.; Lee, Y. One-Pot Electrodeposition of Cobalt Flower-Decorated Silver Nanotrees for Oxygen Reduction Reaction. Appl. Surf. Sci. **2017**, 394, 267–274.

(7) Li, J.; Fa, W.; Zhao, H.; Zhu, C.; Jia, H.; Gu, L. Dendritic Silver Hierarchical Structures for Anode Materials in Li Ion Batteries. Micro Nano Lett. **2019**, 14, 887–891.

(8) Wang, K.; Huang, H.; Han, Y. Quantifying the Driving Force of Silver Crystallization by Chemical Potential Difference. Ind. Eng. Chem. Res. **2021**, 60, 14447–14454.

(9) Amin, M. U.; Zhang, L.; Hao, R.; Zhang, D.; You, H.; Fang, J. Electrochemical Growth of Dendritic Silver Nanostructures as Facile SERS Substrates. Cryst. Eng. Comm. **2021**, 23, 694–699.

(10) Gamburg, Y. D.; Zangari, G. Theory and Practice of Metal Electrodeposition; Springer-Verlag: New York, USA, 2011.

(11) Che, P.; Liu, W.; Chang, X.; Wang, A.; Han, Y. Multifunctional Silver Film with Superhydrophobic and Antibacterial Properties. Nano Research **2016**, 9, 442–450.

(12) Yang, T.; Han, Y. Quantitatively Relating Diffusion and Reaction for Shaping Particles. Cryst. Growth Des. **2016**, 16, 2850–2859.

(13) Taleb, A.; Mangeney, C.; Ivanova, V. Metallic Nanostructure Formation Using Self-Assembled Chemically Anchored Gold Nanoparticles. J. Electrochem. Soc. **2011**, 158, K28–K34.

(14) Taleb, A.; Xue, Y. Electrodeposition of Self Organized Superstructure of Copper Dendrites or Polyhedral Particles on Gold Nanoparticle Modified Highly Oriented Pyrolytic Graphite Electrode. Electrochim. Acta **2013**, 112, 838–844.

(15) Taleb, A.; Xue, Y.; Munteanu, S.; Kanoufi, F.; Dubot, P. Self-Assembled Thiolate Functionalized Gold Nanoparticles Template Toward Tailoring the Morphology of Electrochemically Deposited Silver Nanostructure. Electrochim. Acta **2013**, 88, 621–631.

(16) Qiu, R.; Zhang, D.; Wang, P.; Zhang, X. L.; Kang, Y. S. Tunable Electrochemical Preparation of Cobalt Micro/Nanostructures and Their Morphology-Dependent Wettability Property. Electrochim. Acta **2011**, 58, 699–706.

(17) Yanpeng, X.; Taleb, A.; Jegou, P. Electrodeposition of Cobalt Films With an Oriented Fir Tree-Like Morphology with Adjustable Wetting Properties Using a Self-Assembled Gold Nanoparticle Modified HOPG Electrode. J. Mater. Chem. A **2013**, 1, 11580.

(18) Xu, L.; Karunakaran, R. G.; Guo, J.; Yang, S. Transparent, Superhydrophobic Surfaces from One-Step Spin Coating of Hydrophobic Nanoparticles. ACS Appl. Mater. Interfaces **2012**, 4, 1118–1125.

(19) Darmanin, T.; de Givenchy, E. T.; Amigoni, S.; Guittard, F. Superhydrophobic surfaces by electrochemical processes. Adv. Mat. **2013**, 25, 1378–1394.

(20) Gründer, Y.; Markovic, N. M.; Thompson, P.; Lucas, C. A. Temperature Effects on the Atomic Structure and Kinetics in Single Crystal Electrochemistry. Surf. Sci. **2015**, 631, 123–129.

(21) Ustarroz, J.; Hammons, J. A.; Altantzis, T.; Hubin, A.; Bals, S.; Terryn, H. A Generalized Electrochemical Aggregative Growth Mechanism. J. Am. Chem. Soc. **2013**, 135, 11550–11561.

(22) Desai, D.; Turney, D. E.; Anantharaman, B.; Steingart, D. A.; Banerjee, S. Morphological Evolution of Nanocluster Aggregates and Single Crystals in Alkaline Zinc Electrodeposition. J. Phys. Chem. C **2014**, 118, 8656–8666.

(23) Schiavi, P. G.; Altimari, P.; Zanoni, R.; Pagnanelli, F. Morphology-Controlled Synthesis of Cobalt Nanostructures by Facile Electrodeposition: Transition from Hexagonal Nanoplatelets to Nanoflakes. Electrochim. Acta **2016**, 220, 405–416.

(24) Xu, S.; Zhu, Y.; Xiong, D.; Wang, L.; Yang, P.; Chu, P. K. Zinc Electrodeposition on Polycrystalline Copper: Electrochemical Study of Early-Stage Growth Mechanism. J. Phys. Chem. C **2017**, 121, 3938–3946.

(25) Ustarroz, J. Current Atomic-Level Understanding of Electrochemical Nucleation and Growth on Low-Energy Surfaces. Curr. Opin. Electrochem. **2020**, 19, 144–152.

(26) Yang, Z.; Lv, C.; Li, W.; Wu, T.; Zhang, Q.; Tang, Y.; Shao, M.; Wang, H. Revealing the Two-Dimensional Surface Diffusion Mechanism for Zinc Dendrite Formation on Zinc Anode. Small **2021**, 2021, 2104148.

(27) Zhang, Q.; Wan, J.; Shangguan, J.; Betzler, S.; Zheng, H. Influence of Sub-Zero Temperature on Nucleation and Growth of Copper Nanoparticles in Electrochemical Reactions. iScience **2021**, 24, 103289.

(28) Fukami, K.; Nakanishi, S.; Yamasaki, H.; Tada, T.; Sonoda, K.; Kamikawa, N.; Tsuji, N.; Sakaguchi, H.; Nakato, Y. General Mechanism for the Synchronization of Electrochemical Oscillations and Self-Organized Dendrite Electrodeposition of Metals with Ordered 2D and 3D Microstructures. J. Phys. Chem. C **2007**, 111, 1150–1160.

(29) Nishikawa, K.; Chassaing, E.; Rosso, M. Evolution of the Morphology of Electrodeposited Copper at the Early Stage of Dendritic Growth. J. Electrochem. Soc. **2013**, 160, D183–D187.

(30) Fang, J.; Ma, X.; Cai, H.; Song, X.; Ding, B.; Guo, Y. Double-Interface Growth Mode of Fractal Silver Trees within Replacement Reaction. Appl. Phys. Lett. **2006**, 89, 173104.

(31) Fang, J.; Ding, B.; Song, X.; Han, Y. How a Silver Dendritic Mesocrystal Converts to a Single Crystal. Appl. Phys. Lett. **2008**, 92, 173120.

(32) Aryanfar, A.; Brooks, D. J.; Colussi, A. J.; Merinov, B. V.; Goddard, W. A., III; Hoffmann, M. R. Thermal Relaxation of Lithium Dendrites. Phys. Chem. Chem. Phys. **2015**, 17, 8000–8005.

(33) Aogaki, R.; Makino, T. Morphological Instability in Nonsteady Galvanostatic Electrodeposition I. Effect of Surface Diffusion of Adatoms. J. Electrochem. Soc. **1984**, 131, 40–46.

(34) Castro, M.; Cuerno, R.; Sánchez, A.; Domínguez-Adame, F. Anomalous Scaling in a Nonlocal Growth Model in the Kardar-Parisi-Zhang Universality Class. Phys. Rev. E **1998**, 57, R2491–R2494.

(35) Castro, M.; Cuerno, R.; Sanchez, A.; Dominguez-Adame, F. Multiparticle Biased Diffusion-Limited Aggregation with Surface Diffusion: A Comprehensive Model of Electrodeposition. Phys. Rev. E **2000**, 62, 161–173.

(36) Brandt, I. S.; Zoldan, V. C.; Stenger, V.; Cid, C. C. P.; Pasa, A. A.; Oliveira, T. J.; Reis, F. D. A. A. Substrate Effects and Diffusion Dominated Roughening in Cu_2o Electrodeposition. J. Appl. Phys. **2015**, 118, 145303.

(37) Aarão Reis, F. D. A.; di Caprio, D.; Taleb, A. Crossover from Compact to Branched Films in Electrodeposition with Surface Diffusion. Phys. Rev. E **2017**, 96, 022805.

(38) Hao, F.; Verma, A.; Mukherjee, P. P. Mesoscale Complexations in Lithium Electrodeposition. ACS Appl. Mater. Interfaces **2018**, 10, 26320–26327.

(39) di Caprio, D.; Taleb, A.; Aarão Reis, F. D. A. Effect of Adsorbate Diffusion on the Dendritic Morphology of Electrodeposited Films. J. Phys. Chem. C **2018**, 122, 21418–21432.

(40) Vishnugopi, B. S.; Hao, F.; Verma, A.; Mukherjee, P. P. Surface Diffusion Manifestation in Electrodeposition of Metal Anodes. Phys. Chem. Chem. Phys. **2020**, 22, 11286–11295.

(41) Byun, K.; Saha, J. K.; Jang, J. Role of a Solid-Electrolyte Interphase in the Dendritic Electrodeposition of Lithium: A Brownian Dynamics Simulation Study. J. Phys. Chem. C **2020**, 124, 9134–9141.

(42) Taleb, A.; Yanpeng, X.; Dubot, P. Self-Organized Gold Nanoparticles Modified Hopg Electrodes: Electrochemical Stability and its Use for Electrochemical Nanosensing Applications. Appl. Surf. Sci. **2017**, 420, 110–117.

(43) Zheng, N.; Fan, J.; Stucky, G. D. One-Step One-Phase Synthesis of Monodispersenoble-Metallic Nanoparticles and Their Colloidal Crystals. J. Am. Chem. Soc. **2006**, 128, 6550–6551.

(44) Bain, C. D.; Troughton, E. B.; Tao, Y.-T.; Evall, J.; Whitesides, G. M.; Nuzzo, R. G. Formation of Monolayer Films by the Spontaneous Assembly of Organic Thiols from Solution onto Gold. J. Am. Chem. Soc. **1989**, 111, 321–335.

(45) Fang, J.; You, H.; Kong, P.; Ding, B.; Song, X. Size-Dependent Structure Transformation from Amorphous Phase to Crystal. Appl. Phys. Lett. **2008**, 92, 143111.

(46) Aarão Reis, F. D. A. Dynamic Scaling in Thin-Film Growth with Irreversible Step-Edge Attachment. Phys. Rev. E **2010**, 81, 041605.

(47) To, T. B. T.; de Sousa, V. B.; Reis, F. D. A. A. Thin Film Growth Models with Long Surface Diffusion Lengths. Physica A: Statistical Mechanics and its Applications **2018**, 511, 240 – 250.

(48) Carrasco, I. S. S.; Oliveira, T. J. Height Fluctuations in Homoepitaxial Thin Film Growth: A Numerical Study. Phys. Rev. Res. **2020**, 2, 013385.

(49) Hamdi, R.; Rached, A.; Massoudi, I.; Al-Zuraie, R.; Al-Hamadah, K.; Al-Otaibi, A.; Flemban, T.; Alonizan, N.; Ghrib, T. Electrodeposition Study of Silver: Nucleation Process and Theoretical Analysis. J. Electronic Mater. **2021**, 50, 5507–5513.

(50) Lai, S. C. S.; Lazenby, R. A.; Kirkmana, P. M.; Unwin, P. R. Nucleation, Aggregative Growth and Detachment of Metal Nanoparticles During Electrodeposition at Electrode Surfaces. Chem. Sci. **2015**, 6, 1126–1138.

(51) Chan, P.; Dow, W. Spontaneous Potential Oscillation Resulting in Copper Deposit with Ultra-Large Grains. J. Electrochem. Soc. **2019**, 166, D891–D897.

(52) Wang, K.; Chen, Y.; Dou, X.; Han, Y. The Role of Interface Concentration Gradient in the Formation of Silver Dendritic Particles. Adv. Powder Technol. **2021**, 32, 1766–1773.

(53) Meakin, P. Diffusion-Controlled Deposition on Fibers and Surfaces. Phys. Rev. A **1983**, 27, 2616–2623.

(54) Witten, T. A.; Sander, L. M. Diffusion-Limited Aggregation, a Kinetic Critical Phenomenon. Phys. Rev. Lett. **1981**, 47, 1400–1403.

(55) Luis, E. E. M.; Carrasco, I. S. S.; de Assis, T. A.; Aarão Reis, F. D. A. Statistics of Adatom Diffusion in a Model of Thin Film Growth. Phys. Rev. E **2020**, 102, 012805.

(56) Mamme, M. H.; Köhn, C.; Deconinck, J.; Ustarroz, J. Numerical Insights into the Early Stages of Nanoscale Electrodeposition: Nanocluster Surface Diffusion and Aggregative Growth. Nanoscale **2018**, 10, 7194–7209.

(57) Zhang, C.-M.; Bartelt, M. C.; Wen, J.-M.; Jenks, C. J.; Evans, J. W.; Thiel, P. A. Submonolayer Island Formation and the Onset of Multilayer Growth During Ag/Ag(100) Homoepitaxy. Surf. Sci. **1998**, 406, 178–193.

(58) Evans, J.; Thiel, P.; Bartelt, M. Morphological Evolution During Epitaxial Thin Film Growth: Formation of 2D Islands and 3D Mounds. Surface Science Reports **2006**, 61, 1 – 128.

(59) Brune, H.; Bromann, K.; Roder, H.; Kern, K.; Jacobsen, J.; Jacobsen, K.; Norskov, J. Effect of Strain on Surface Diffusion and Nucleation. Phys. Rev. B **1995**, 52, R14380–R14383.

(60) Jiang, Z.; Lin, Y.; Xie, Z. Structural Investigations and Growth Mechanism of Well-Defined Ag Dendrites Prepared by Conventional Redox Displacement. Mater. Chem. Phys. **2012**, 134, 762–767.

(61) Radmilović, V. V.; Kacher, J.; Ivanović, E. R.; Minor, A. M.; Radmilović, V. R. Multiple Twinning and Stacking Faults in Silver Dendrites. Cryst. Growth Des. **2016**, 16, 467–474.

(62) Erlebacher, J. An Atomistic Description of Dealloying - Porosity Evolution, the Critical Potential, and Rate-Limiting Behavior. J. Electrochem. Soc. **2004**, 151, C614–C626.

(63) Hernandez, T. S.; Barile, C. J.; Strand, M. T.; Dayrit, T. E.; Slotcavage, D. J.; McGehee, M. D. Bistable Black Electrochromic Windows Based on the Reversible Metal Electrodeposition of Bi and Cu. ACS Energy Lett. **2018**, 3, 104–111.

(64) Eh, A. L.-S.; Chen, J.; Zhou, X.; Ciou, J.-H.; Lee, P. S. Robust Trioptical-State Electrochromic Energy Storage Device Enabled by Reversible Metal Electrodeposition. ACS Energy Lett. **2021**, 6, 4328–4335.

(65) Tao, X.; Liu, D.; Yu, J.; Cheng, H. Reversible Metal Electrodeposition Devices: An Emerging Approach to Effective Light Modulation and Thermal Management. Adv. Optical Mater. **2021**, 9, 2001847.

TOC Graphic

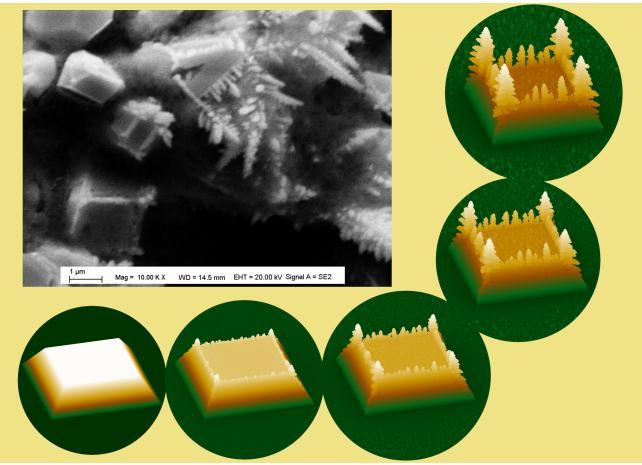

Supporting Information
Effects of Adsorbate Diffusion and Edges in a Transition from Particle to Dendritic Morphology During Silver Electrodeposition

Sohère Dokhan[1,2], Dung di Caprio[2], Abdelhafed Taleb[2], and Fábio D. A. Aarão Reis*[3]

[1]PSL Research University, Chimie ParisTech - CNRS, Institut de Recherche de Chimie Paris, 75005, Paris, France

[2]Unité de Recherche Matériaux, Procédés et Environnement URMPE, Université M'hamed Bougara de Boumerdés, Faculté des Sciences, Boumerdés, Algérie

[3]Instituto de Física, Universidade Federal Fluminense, Avenida Litorânea s/n, 24210-340 Niterói, RJ, Brazil

*fdaar@protonmail.com

SI.I Justification of the Model

The relaxation of adatoms and nanoclusters at the tips of silver dendrites during the electrodeposition was formerly shown in transmission electron microscopy (TEM) studies [1, 2]. The tips are formed by crystalline cores surrounded by amorphous layers with thicknesses of some nanometers. The core grows by crystallization in the amorphous layer. Nanograins may also form in that layer and are incorporated to the core after rotation and realignment. Simultaneously, there is deposition of material at the interface between the amorphous layer and the electrolyte. This mechanism was termed double interface growth mode [1] and is supported by molecular dynamics simulations [3]. The diffusion of atoms in the amorphous layer and the relaxation of nanograins are necessary ingredients for the formation of self-organized structures, otherwise random (DLA-like) aggregates would be formed. However, the absence of relaxation of the crystallized material is necessary for the stability of the dendrite shape while the growth continues.

Our model for the hops of mobile particles describes the diffusion of the atoms in the amorphous layers and in the neighborhood of the crystal surface. The formation of a new atomic layer of the crystal is possible due to the incorporation of the atoms in this neighborhood. The atom mobility in these conditions is quantitatively represented by the parameters G and P. It is reasonable to assume that incorporation of an atom to the crystal preferentially occurs at the positions of the crystal surface with the highest coordinations; this justifies the decrease of P_{hop} as n increases [Eq. (1) of the main text with $P < 1$]. The model also sets a limitation in the number of hop attempts of a mobile atom. This implies that the relaxation occurs in a finite time interval between the cation reduction and the final incorporation to the crystal; in these conditions, there is no relaxation of the previously formed crystal.

SI.II Simulation Method

To model the diffusion of a cation in the electrolyte, the cation is released at a position $(x, y, h_{max} + 45d)$ with randomly chosen x and y and with h_{max} defined as the maximal value of z of a previously aggregated atom (including the electrode). The cation executes an unbiased random walk (RW) to nearest neighbor (NN) sites in the electrolyte, as illustrated in Fig. 1(a) of the main text. During this motion, the position z cannot exceed $h_{max}+45d$ to prevent that the cation moves to regions far from the substrate. The diffusive cation motion is a reasonable approximation when the concentration near the film surface is very small.

The dimensionless simulation time T is the ratio between the number of deposited particles and the number of sites of the base of the simulation cell (so it is meaninful only in the case of deposition on flat electrodes). The simulations on flat electrodes and on large seeds were performed in cells with lateral size $L = 1536d$ until the maximal height reached the value $h_{max} = 1480d$. Several values of G from 5×10^2 to 5×10^4 were considered and the values of P were between 0.025 and 0.3. For each parameter set, 10–20 different deposits were grown, which allows the calculation of accurate dendrite sizes.

The simulations of growth with small seeds used cells of lateral size $L = 1448d$. This corresponds to a practical choice of indexing where the points of constant z plane are located in a matrix 1024×2048. Since these simulations were constrained to shorter growth times, values of G up to 1×10^8 were considered, with P betweeen 0.01 and 0.3. The unit dimensionless time in the simulations with small seeds corresponds to the release of 512 cations. 10–20 different deposits were also grown for each parameter set.

In the main text and in the remaining part of this supplement, all simulation results are presented with lengths in units of the distance d.

The simulations were run on Nvidia Tesla K80 graphic cards or commercial GTX 1080 Ti or 2080 Ti cards in the CUDA environment for parallelization. In each simulation step, 512 cations are simultaneously released above the deposit. In this parallel process, more than one mobile atom may reach the same final site due to the slow update of the memory, which does not signal that site as being already occupied. In such case, the actual number of deposited particles is counted and the missing number due to multiple particles on the same site is added by performing supplementary depositions. This case is more frequent when P is small and at sites with a large number of neighbours, in which the residence time of a mobile atom is large.

SI.III Current Fluctuations and Particle Growth

Fig. S1 shows an additional FEGSEM image obtained after 600s of electrodeposition. It shows a larger number of silver particles than Figs. 4(a) and 4(b) of the main text. Some regions with dendrites are marked. The particle sizes range from some tenths of micrometers to 1–2μm (with the image resolution, it is difficult to identify particle sizes $< 0.1\mu$m). The size polydispersity shows that new particles nucleate throughout the whole electrodeposition time, with apparently uniform spatial distribution on the Au NP modified HOPG electrode.

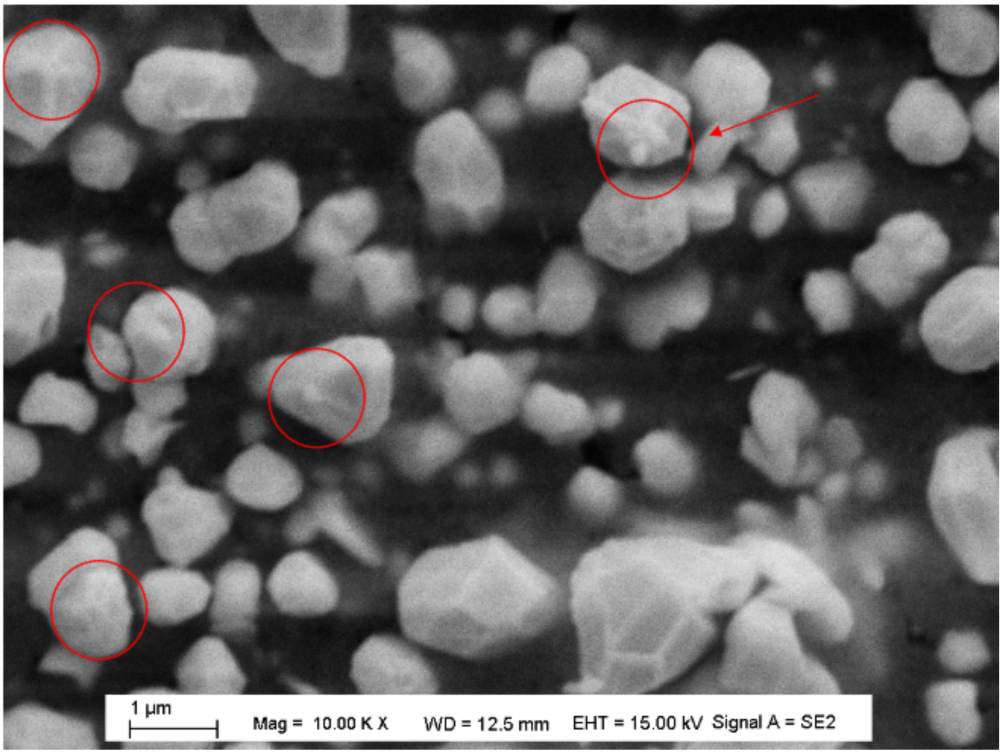

Figure S1: FEGSEM image of the silver electrodeposit after 600s of deposition.

The progressive nucleation of nanoparticles and microparticles is also observed in other electrodeposition processes and explains fluctuations in the current (in potentiostatic deposition) or in the potential (in galvanostatic deposition). Lai et al [4] studied the initial stages of silver nanoparticle electrodeposition on HOPG electrodes in potentiostatic conditions. The current densities were of order 0.01mA/cm^2 and showed oscillations with periods ~ 0.01s, which were associated with the formation of nanoparticles of size $\sim 20nm$. Chan et al [5] performed galvanostatic deposition of polycrystalline copper films, with current densities of order 0.1mA/cm^2. In a growth stage where grains of sizes 20–50μm were formed, oscillations

in the potential were observed, with periods 250–500s.

In our electrodeposition experiment, the sizes of silver particles are intermediate between those of the above experiments and so are the periods of the oscillations (typically 5–10s in Fig. 3 of the main text). This gives additional support to the relation between those oscillations and the growth of particles or crystalline grains. The simplest interpretation of this relation is that the surface area for cation reduction changes while the particles or grains grow, but other mechanisms may also contribute to current oscillations (e.g. detachment of nanoparticles from the substrate [4]).

SI.IV Calculation of the Nanotree Width in the Simulations

To improve the accuracy of the estimates of the nanotree widths, we consider the samples grown on a flat substrate because each configuration has some tens of tall nanotrees. At heights near 2/3 of the total height of the simulation box, the densities of all deposits reach approximately height independent values, so an interval of values of z around that height is considered to estimate the average widths.

Figs. S2(a)-(b) show examples of cross sections of two deposits with constant z in this region. In such cross sections, the lengths of segments of connected atoms along the x direction are measured (i.e. along all lines with a constant y); periodic boundaries are considered. The average of those lengths represents an average of characteristic widths of the nanotrees. After averaging over five horizontal (constant z) sections of each sample and over different samples, we obtain the average width W. The main contributions to W are observed to come from (i) the distance between opposite tips of secondary branches and (ii) the widths of the secondary branches (whose value is near the width of the trunk).

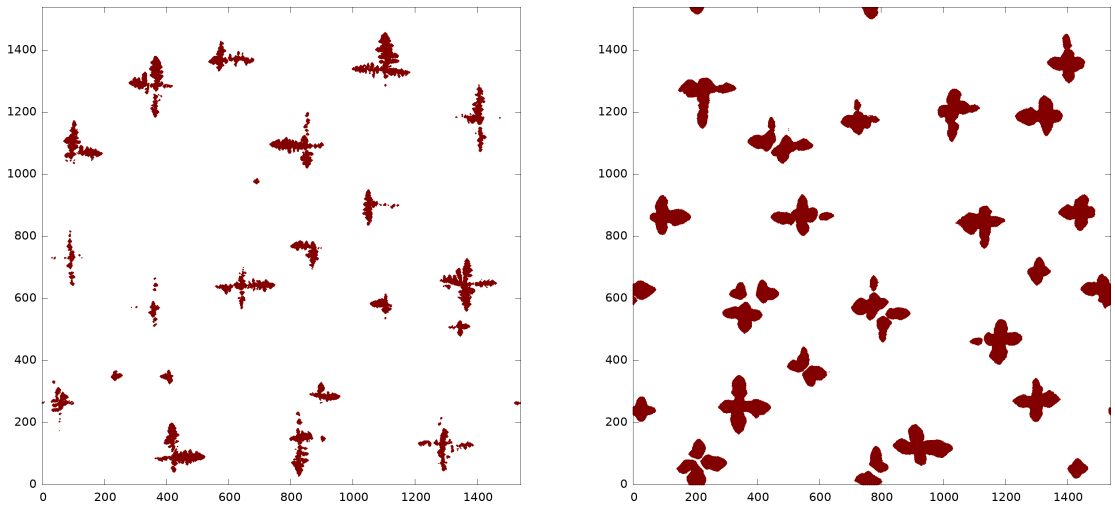

Figure S2: Horizontal cross section of simulated deposits at a height near 2/3 of the maximal height, for: (a) $G = 10^4$, $P = 0.1$; (b) $G = 10^4$, $P = 0.3$.

SI.V Additional Images of Simulated Deposits on Flat Substrates

Fig. S3 compares the effects of changing G and P on the nanotree width. The central panel shows (perspective, top, and lateral) images of a deposit grown with $G = 10^4$ and $P = 0.1$. The left panel shows images of a deposit obtained with a value of G three times larger and the same P. The right panel shows images of a deposit obtained with a value of P three times larger that that of the central panel and the same G. The change in P visibly leads to a larger increase in the widths of the nanotrees.

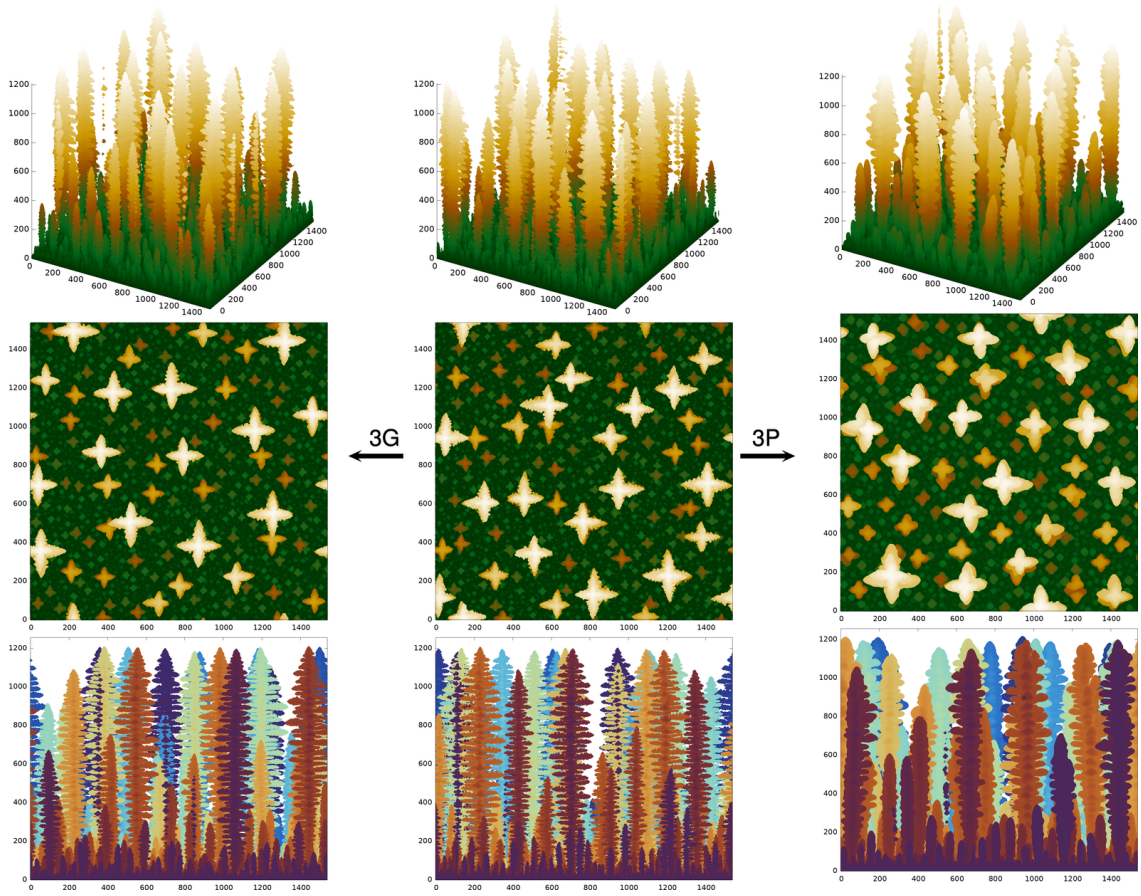

Figure S3: Images of simulated deposits with: $G = 10^4$ and $P = 0.1$ in the center; $G = 3{\times}10^4$ and $P = 0.1$ at the left; $G = 10^4$ and $P = 0.3$ at the right.

SI.VI Top Views of (001) and (111) Surfaces

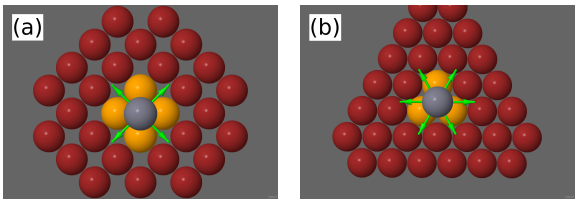

Figure S4: Mobile atoms (gray) on (a) a (001) terrace and (b) a (111) terrace. Possible hops are indicated by green arrows. The NNs of the terraces are highlighted in yellow and the other terrace atoms are in red.

SI.VII Additional Images of Simulated Deposits on Small Seeds

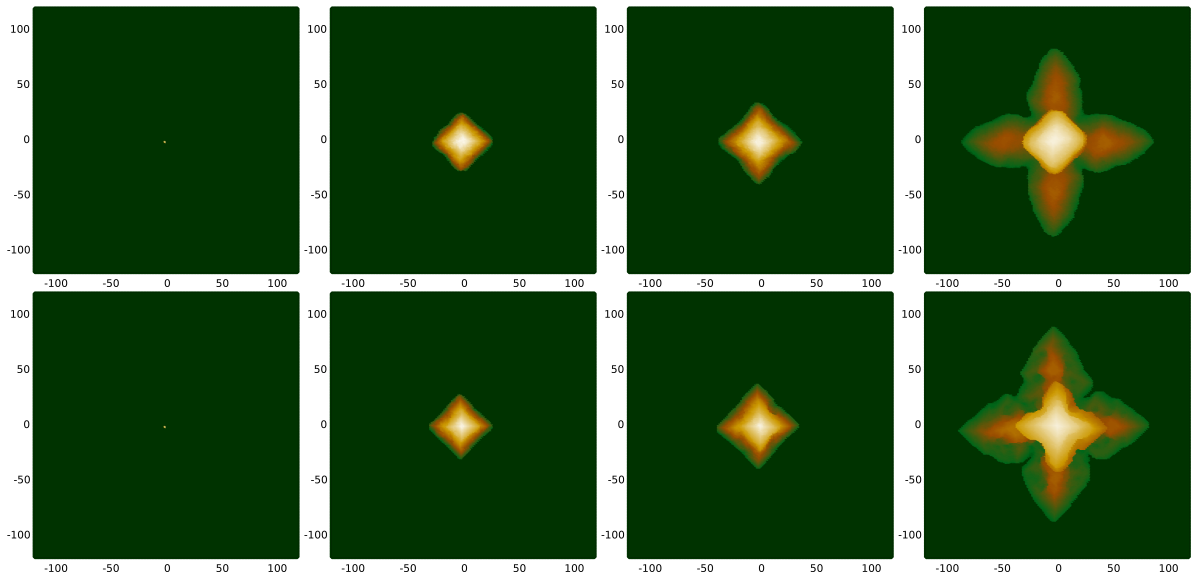

Figure S5: Top views of the deposits grown on a small seed. Top: $G = 5 \times 10^4$, $P = 0.2$ (same as Fig. 8(a) of the main text); from left to right, dimensionless times are $T = 0$, 592, 1248, and 8000 Bottom: $G = 10^6$, $P = 0.05$ (same as Fig. 8(b) of the main text); from left to right, $T = 0$, 1280, 2592, and 172800.

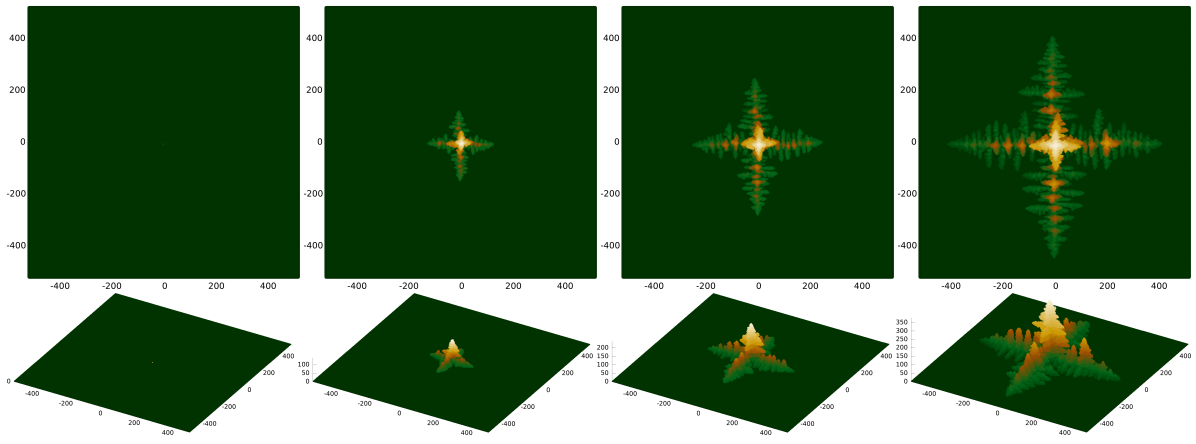

Figure S6: Deposits grown on a small seed with $G = 10^4$ and $P = 0.1$. From left to right, dimensionless times are $T = 0$, 1008, 4080, and 12272.

SI.VIII Calculation of the Transition Size

Fig. S7(a) shows the time evolution of l_d and l_s for the same parameters of the images of Fig. 8(b) of the main text. It shows that l_d increases faster than l_s. This is consistent with the visual inspection of the transition from pyramidal particles to dendrites, in which the lateral edges of the pyramid rapidly propagate in the x and y directions. For other parameter sets, a saturation of l_s may be observed at long times, while l_d still increases.

Fig. S7(b) shows the time evolution of the aspect ratio l_d/l_s. This ratio is equal to $\sqrt{2}$ in a perfect pyramid with lateral $[\pm 1, \pm 1, 1]$ faces. The transition time is obtained at the point where the linear fit of the $l_d/l_s \times T$ plot reaches the value $\sqrt{2}$, as illustrated in Fig. S7(b). The transition length S_t is defined as the value of l_s at that time.

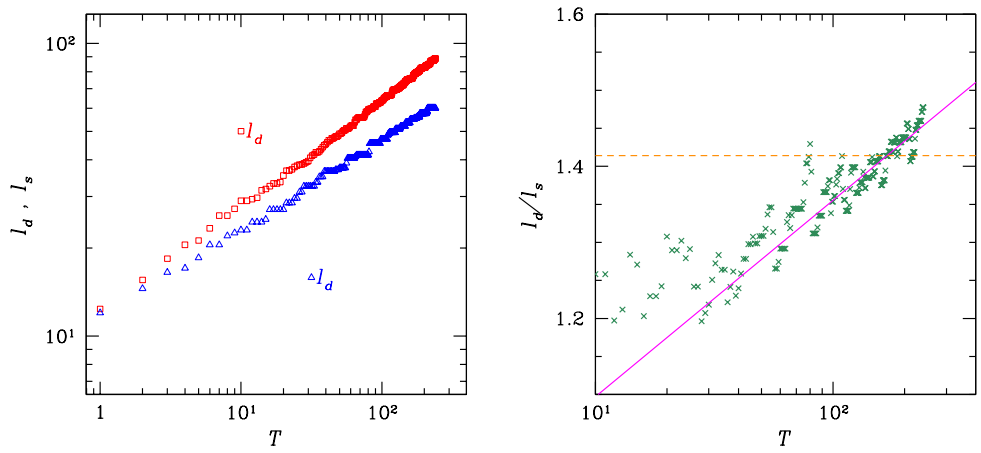

Figure S7: (a) Evolution of diagonal length (red squares) and side length (blue triangles) in simulations with $G = 10^6$ and $P = 0.05$. (b) Evolution of l_d/l_s (green crosses) for the same parameter set and a linear fit (magenta line) near the transition value $\sqrt{2}$ (dashed orange line). All lengths are given in simulation units (half of the lattice constant).

SI.IX Scaling of the Transition Size

Fig. S8(a) shows the slopes α of the fits of the $\log S_t \times \log G$ plots [Fig. 11 of the main text] as a function of P. The linear fit in Fig. S8(a) gives $\alpha = -4.68P + 0.511$ for $0.01 \leq P \leq 0.05$.

Fig. S8(b) shows the intercepts β of the fits of the $\log S_t \times \log G$ plots [Fig. 11 of the main text] as a function of P. The linear fit in Fig. S8(b) gives $\beta = 38.7P - 1.78$ for $0.01 \leq P \leq 0.05$.

Considering the deviations of the fits from the data points in Figs. S8(a)-(b), we estimate the uncertainties in the coefficients of those fits to be near 10%.

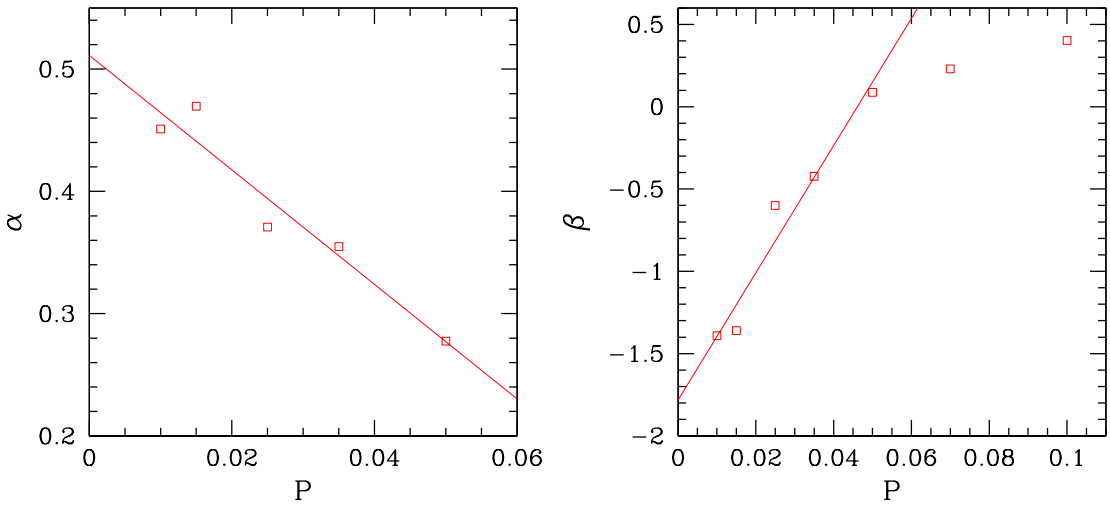

Figure S8: (a) Slopes α and (b) intercepts β of the fits of the $\log S_t \times \log G$ plots as a function of P.

SI.X Simulations with (112)-Oriented Substrate

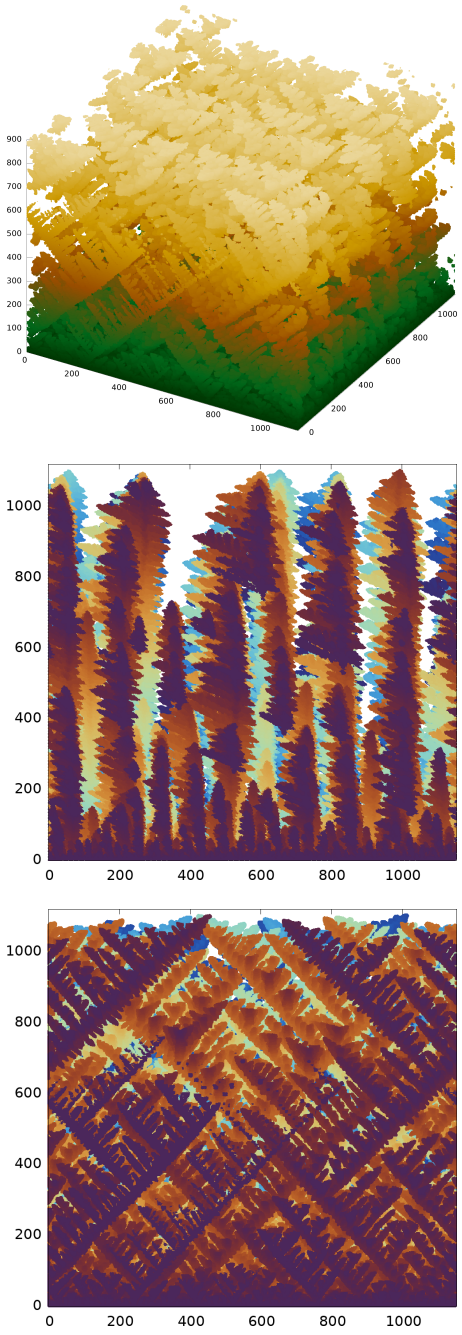

Figure S9: (a) Perspective and (b),(c) lateral views of a deposit simulated with substrate with normal [112] direction and parameters $G = 10^4$, $P = 0.125$.

References

[1] J. Fang, X. Ma, H. Cai, X. Song, B. Ding, and Y. Guo. Double-Interface Growth Mode of Fractal Silver Trees within Replacement Reaction. Appl. Phys. Lett., 89:173104, 2006.

[2] J. Fang, B. Ding, X. Song, and Y. Han. How a Silver Dendritic Mesocrystal Converts to a Single Crystal. Appl. Phys. Lett., 92:173120, 2008.

[3] J. Fang, H. You, P. Kong, B. Ding, and X. Song. Size-Dependent Structure Transformation from Amorphous Phase to Crystal. Appl. Phys. Lett., 92:143111, 2008.

[4] Stanley C. S. Lai, Robert A. Lazenby, Paul M. Kirkmana, and Patrick R. Unwin. Nucleation, Aggregative Growth and Detachment of Metal Nanoparticles During Electrodeposition at Electrode Surfaces. Chem. Sci., 6:1126–1138, 2015.

[5] Po-Fan Chan and Wei-Ping Dow. Spontaneous Potential Oscillation Resulting in Copper Deposit with Ultra-Large Grains. J. Electrochem. Soc., 166:D891–D897, 2019.